The Global Photospheric and Coronal Magnetic Field:

Magnetograph Comparisons and End-to-end Calibration

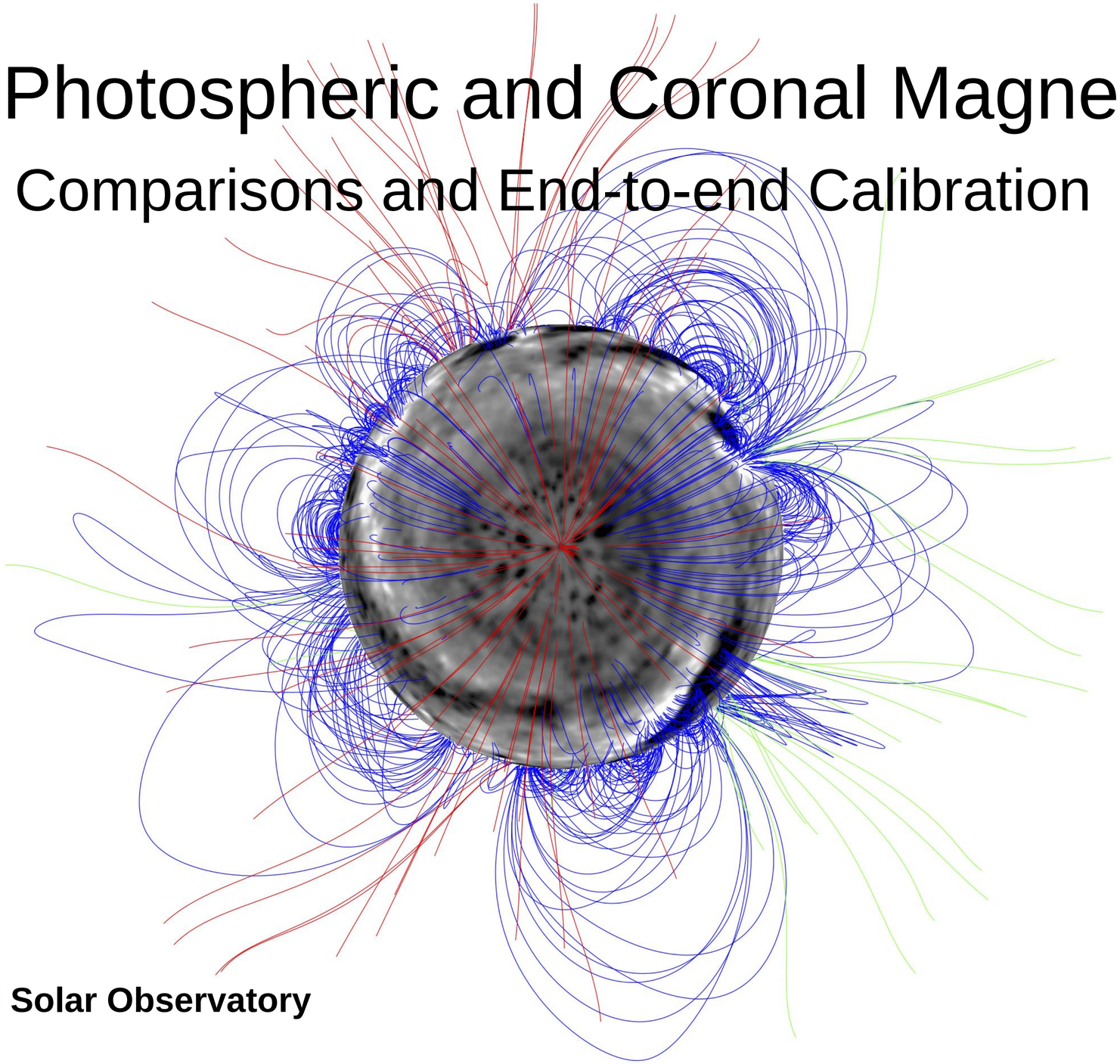

Gordon Petrie, National Solar Observatory

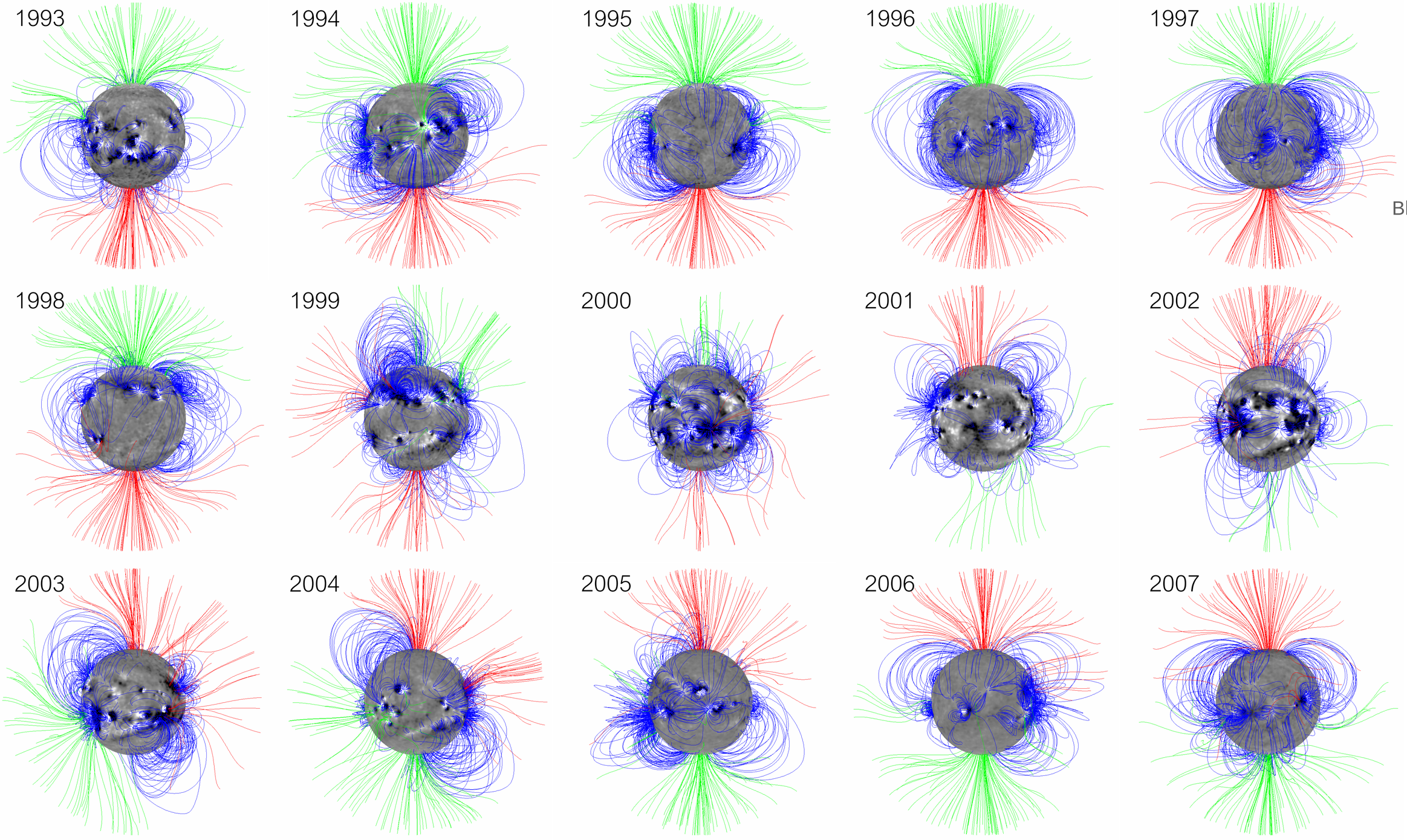
1993
1994
1995
1996
1997
Blah
1998
1999
2000
2001
2002
2003
2004
2005
2006
2007

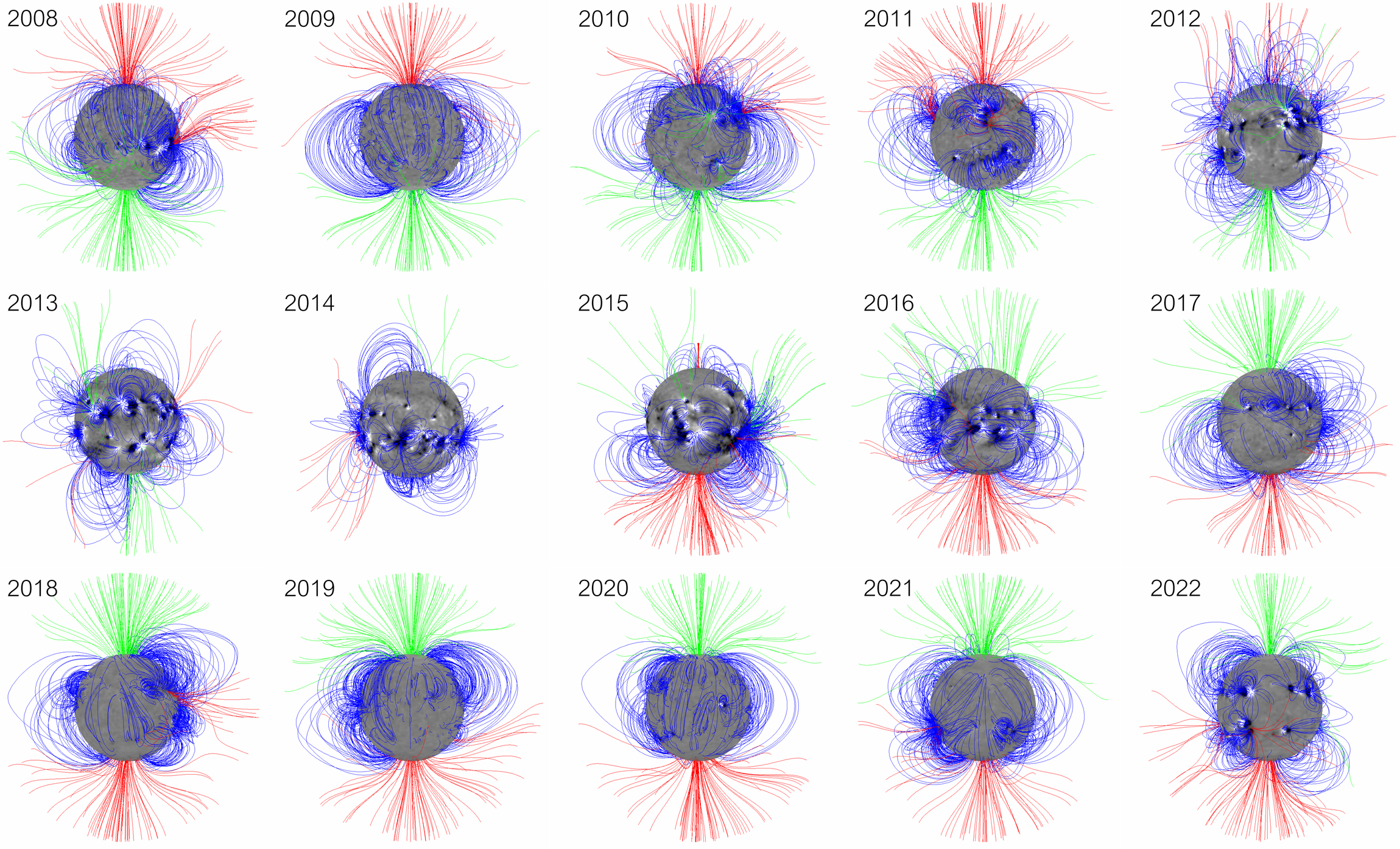
2008
2009
2010
2011
2012
2013
2014
2015
2016
2017
2018
2019
2020
2021
2022

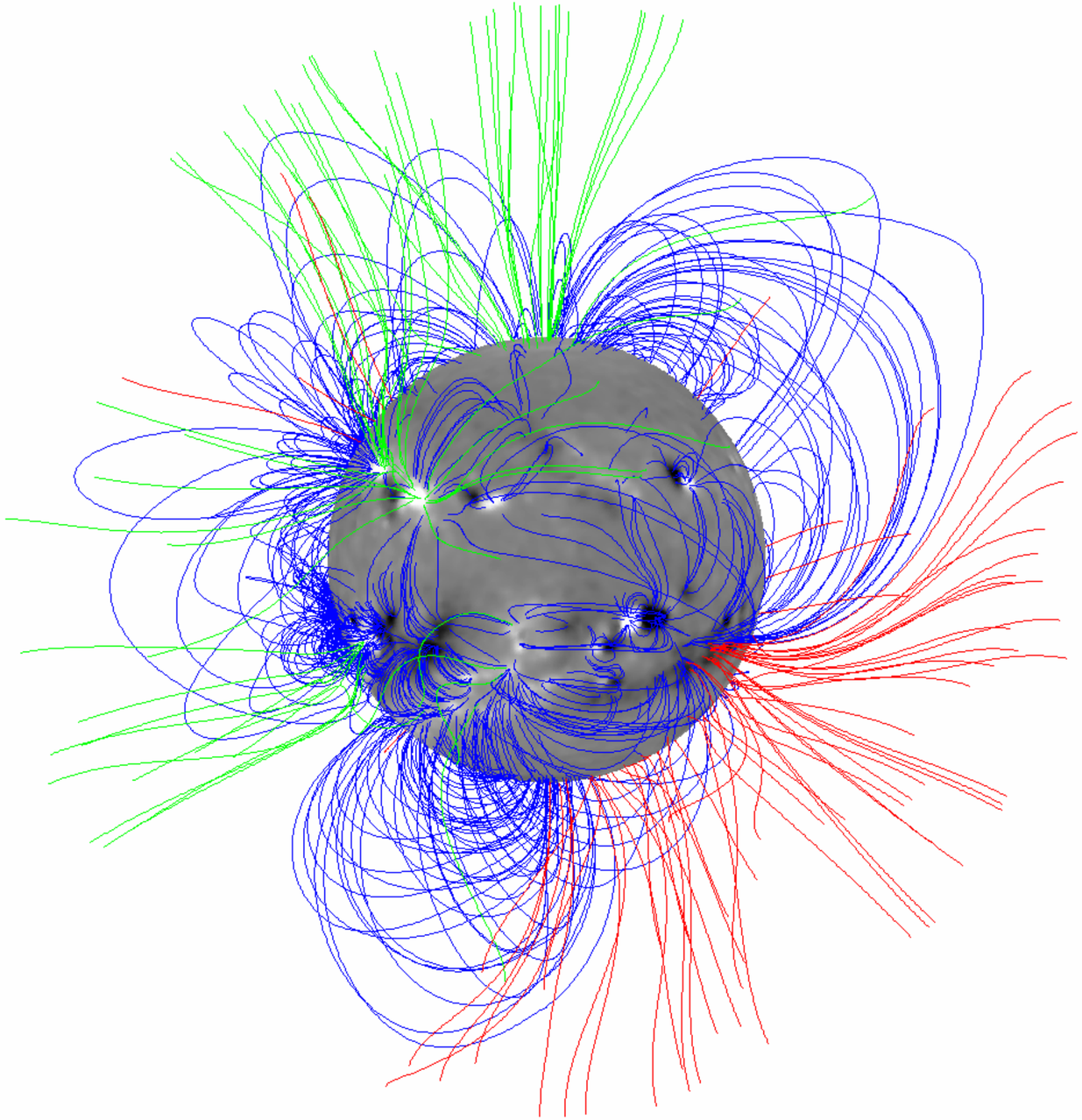

PFSS model (R_{ss} = 2.5 $R_{\odot}$) based on GONG synoptic map for CR 2060 (August 2022).

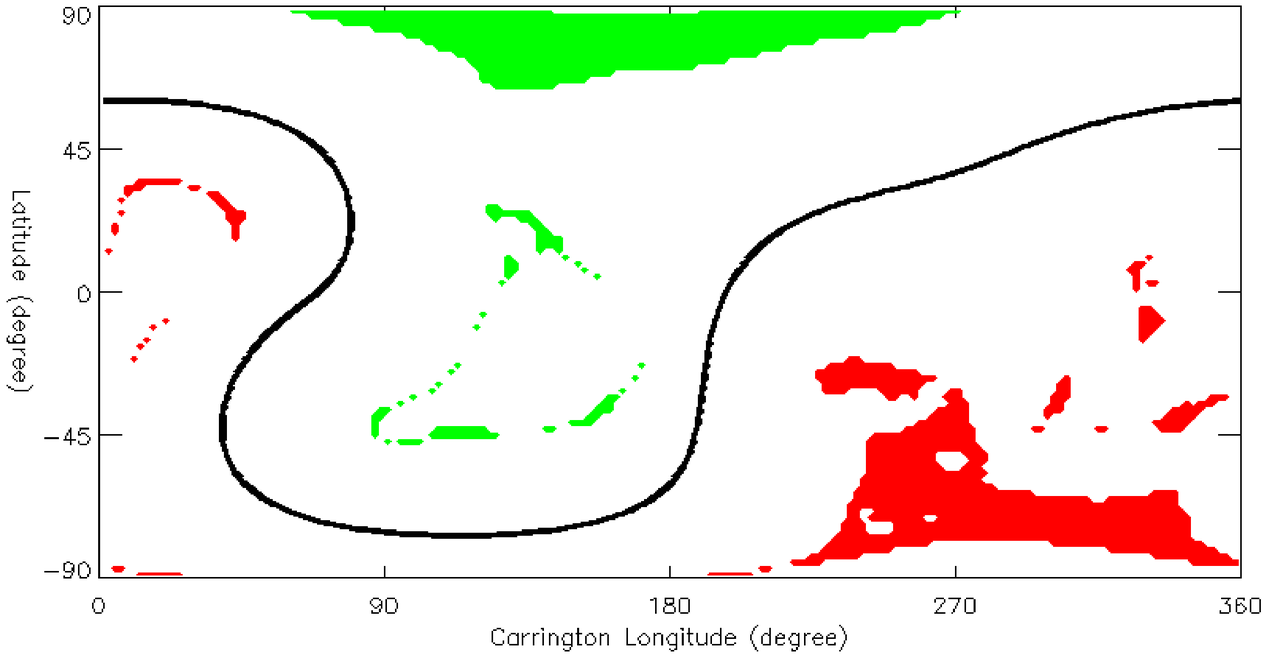

The dipole has become very tilted in recent months, and the PFSS source-surface neutral line has become very warped.

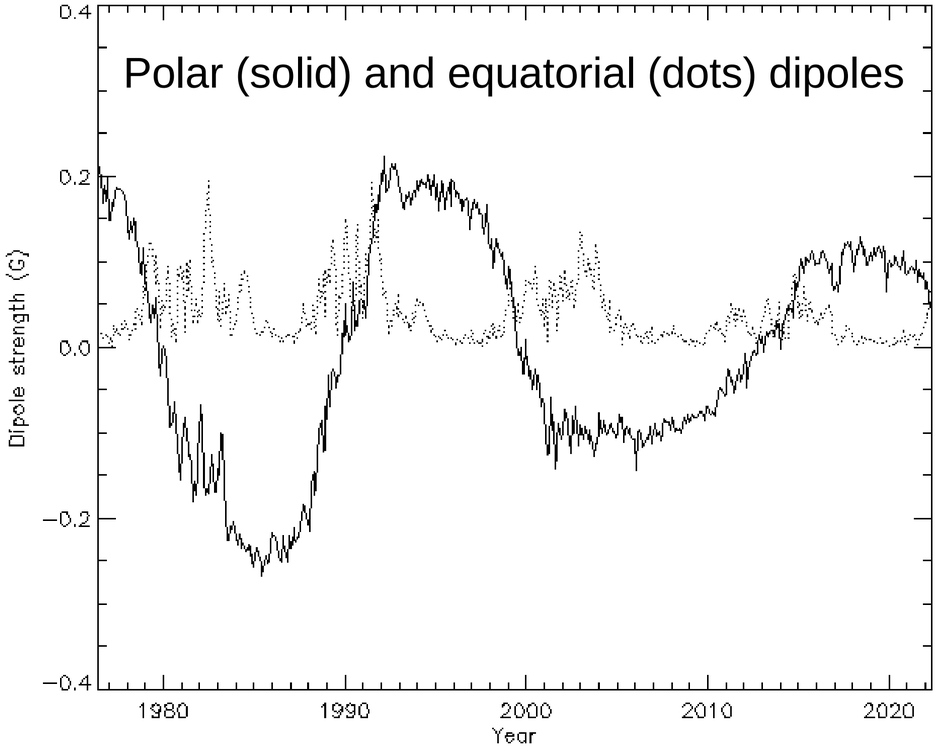

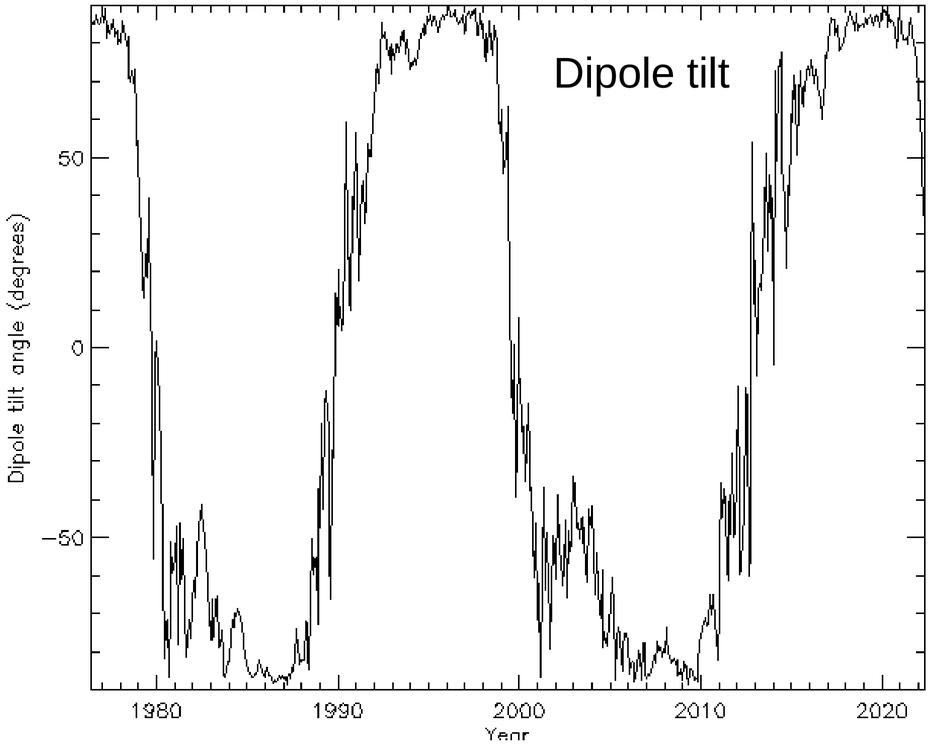

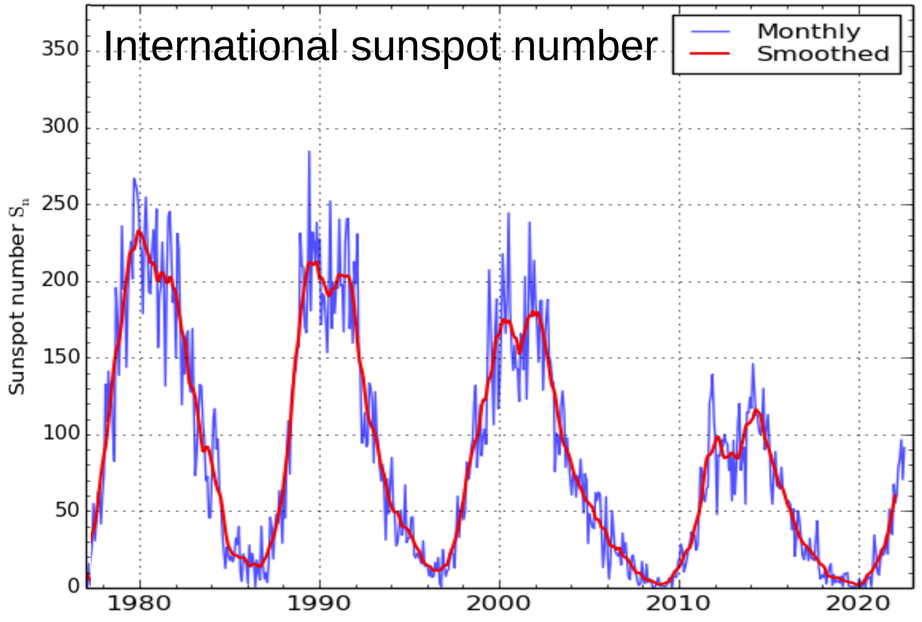

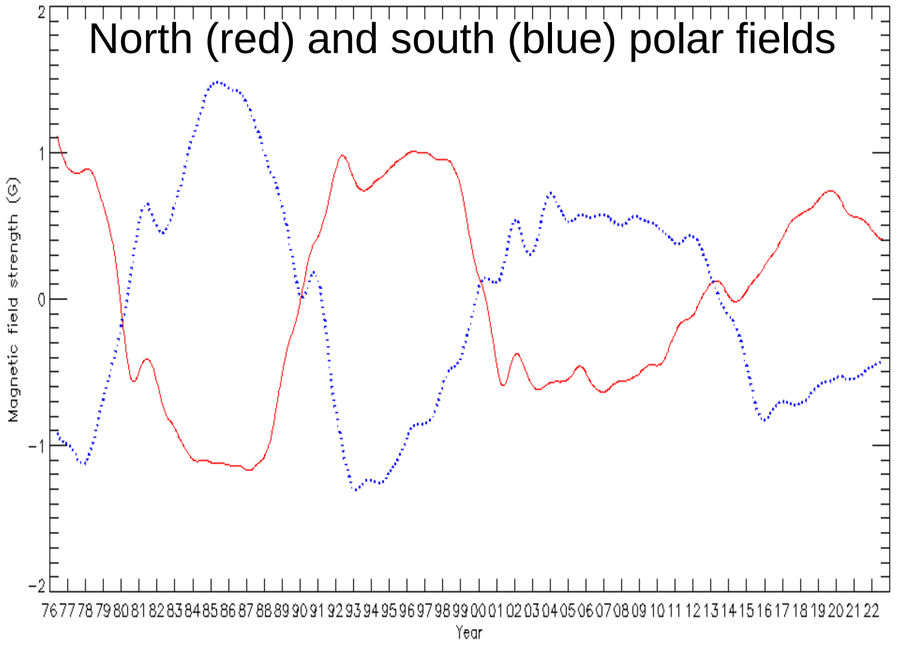

Wilcox Solar Observatory polar and equatorial dipoles (left), dipole tilt (top right), polar fields (bottom right). International sunspot number shown (bottom left) for reference.

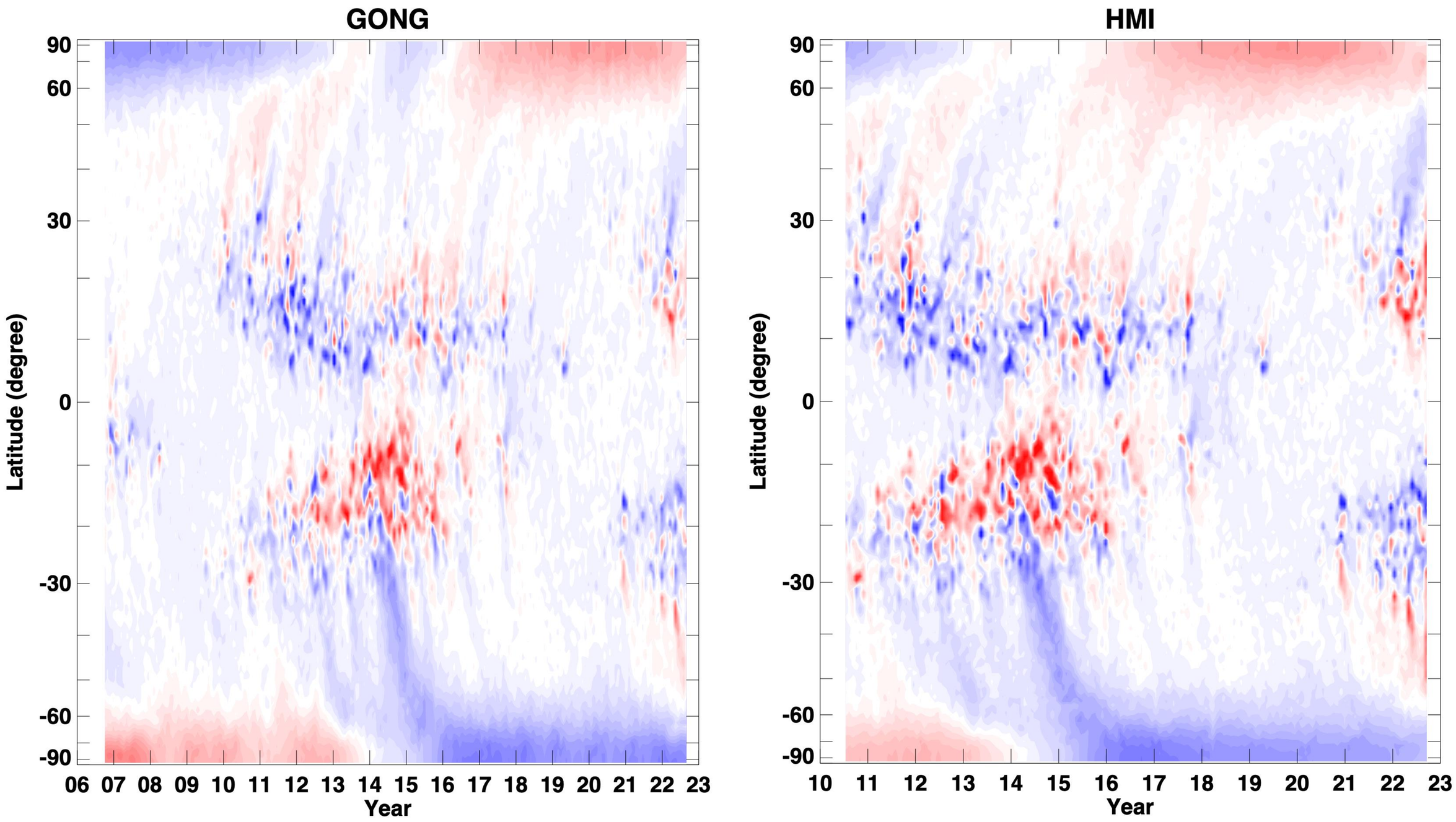

Butterfly diagrams of data from GONG (left) and HMI (right). Red=positive, blue negative, saturates at ±10G.

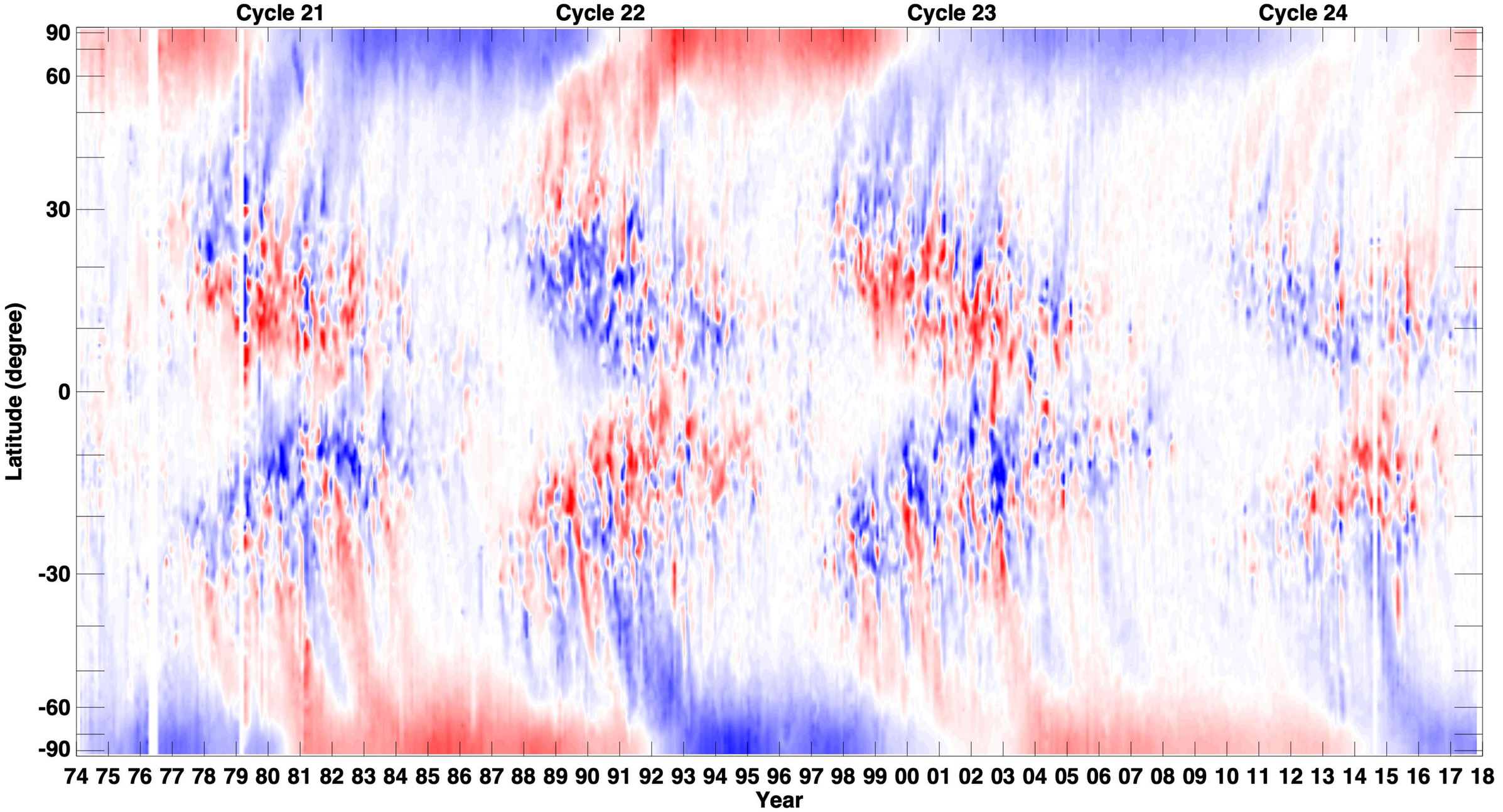

Butterfly diagram of data from KPVT/512ch (74-92), KPVT/SPMG (92-03), and SOLIS/VSM (03-17). Red=positive, blue negative, saturates at ±15G. Polar reversals can be fast (cycle 21, 22) or slow (cycle 23 S, 24 N).

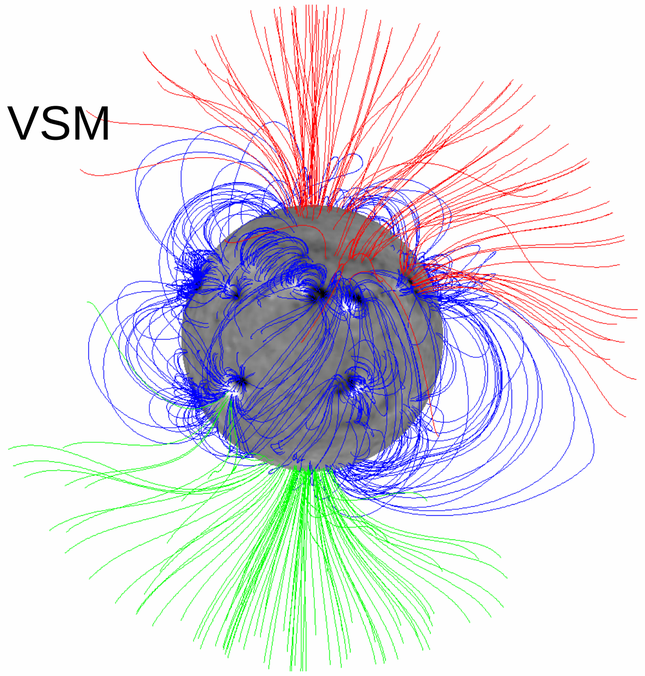

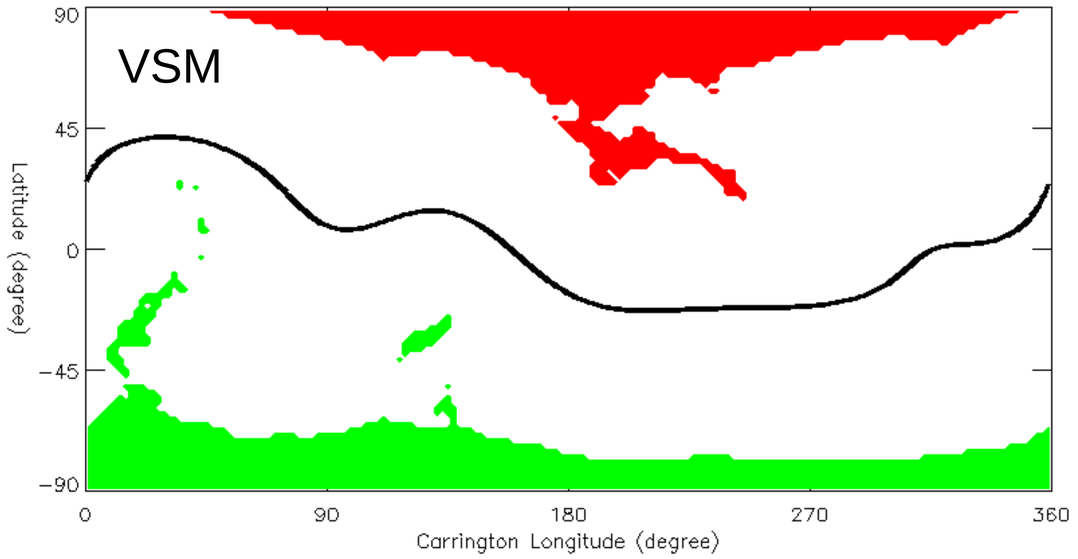

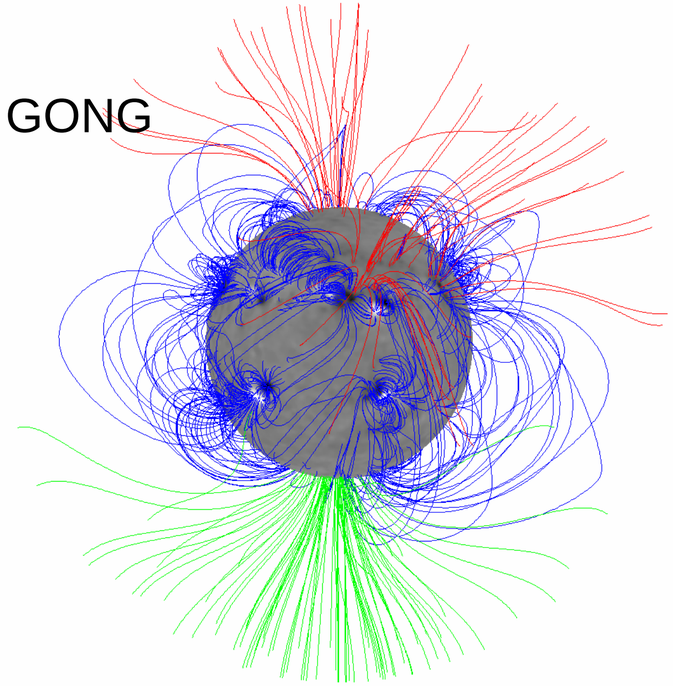

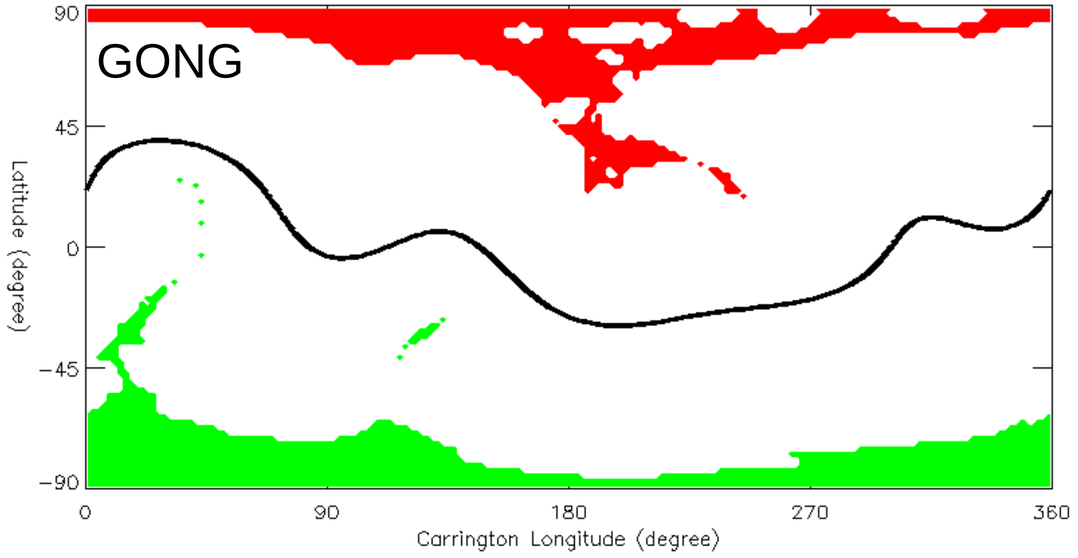

Comparison between VSM and GONG synoptic maps and PFSS models (R_{ss} = 2.5 $R_{\odot}$) for CR 2098.

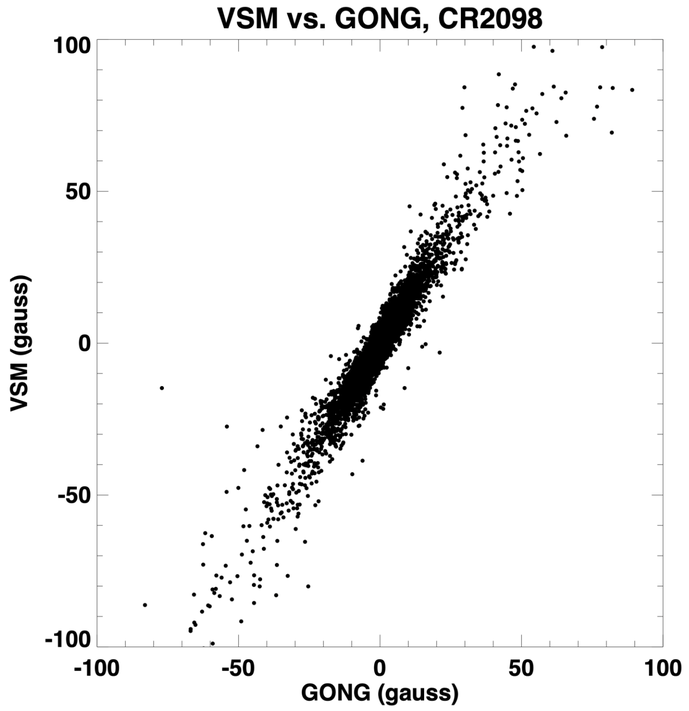

The maps were processed identically at NSO, and there are only minor differences between the models features (left). However, the VSM field values are significantly higher than the GONG ones (above).

‘Open flux problem’: how to resolve the persistent underestimation of the radial interplanetary magnetic field by heliospheric models using surface magnetograms? Table from Linker et al. (2017). See also Virtanen & Mursula (2017).

Table 1
Summary of Results from all of the Model/Map Combinations

1	2	3	4	5	6
Magnetic Map	Unsigned Flux (10^{22} Mx)	Average Polar Field (G) South/North	Model	Open Field Area (Difference) (10^{21} cm^2)	Open Flux (B_r at 1 au, nT)
Observed				7.6 (EUV)	1.7–2.2 (OMNI)
ADAPT, far side	17.9	3.1 (S)	PFSS, 2.5R_{SS}	5.8 (−1.8)	0.75
(NSO VSM magnetograms)		−2.6 (N)	PFSS, 2.0R_{SS}	6.9 (−0.7)	0.94
			MHD	8.9 (+1.3)	1.35
ADAPT, far side	17.6	3.1 (S)	PFSS, 2.5R_{SS}	6.3 (−1.3)	0.82
AR polarity reversed		−2.6 (N)	PFSS, 2.0R_{SS}	7.4 (−0.2)	1.03
			MHD	8.7 (+1.1)	1.33
ADAPT, no far side	14.8	3.1 (S)	PFSS, 2.5R_{SS}	6.1 (−1.5)	0.76
		−2.6 (N)	PFSS, 2.0R_{SS}	7.1 (−0.5)	0.94
			MHD	9.3 (+1.7)	1.28
GONG daily synoptic	11.4	2.6 (S)	PFSS, 2.5R_{SS}	6.0 (−1.6)	0.62
		−2.4 (N)	PFSS, 2.0R_{SS}	7.0 (−0.6)	0.75
GONG synoptic	11.3	2.6 (S)	PFSS, 2.5R_{SS}	6.3 (−1.3)	0.64
		−2.4 (N)	PFSS, 2.0R_{SS}	7.3 (−0.3)	0.77
HMI LOS daily updated	12.9	2.8 (S)	PFSS, 2.5R_{SS}	5.8 (−1.8)	0.66
		−2.7 (N)	PFSS, 2.0R_{SS}	6.7 (−0.9)	0.79
HMI LOS synoptic	13.9	2.9 (S)	PFSS, 2.5R_{SS}	5.4 (−2.2)	0.65
		−2.7 (N)	PFSS, 2.0R_{SS}	6.3 (−1.3)	0.79
HMI vector synoptic	15.1	3.5 (S)	PFSS, 2.5R_{SS}	5.4 (−2.2)	0.80
		−3.7 (N)	PFSS, 2.0R_{SS}	6.3 (−1.3)	0.96
LMSAL ESFAM	13.2	3.9 (S)	PFSS, 2.5R_{SS}	4.3 (−3.3)	0.64
(MDI magnetograms)		−2.4 (N)	PFSS, 2.0R_{SS}	5.3 (−2.3)	0.78
			MHD	7.8 (+0.2)	1.12
MDI daily updated	18.4	3.5 (S)	PFSS, 2.5R_{SS}	4.8 (−2.8)	0.75
		−3.2 (N)	PFSS, 2.0R_{SS}	5.7 (−1.9)	0.92
MDI synoptic	18.2	3.3 (S)	PFSS, 2.5R_{SS}	5.1 (−2.5)	0.73
		−3.2 (N)	PFSS, 2.0R_{SS}	5.9 (−1.7)	0.90
VSM synoptic	16.3	3.4 (S)	PFSS, 2.5R_{SS}	5.5 (−2.1)	0.79
		−3.3 (N)	PFSS, 2.0R_{SS}	6.4 (−1.2)	0.96

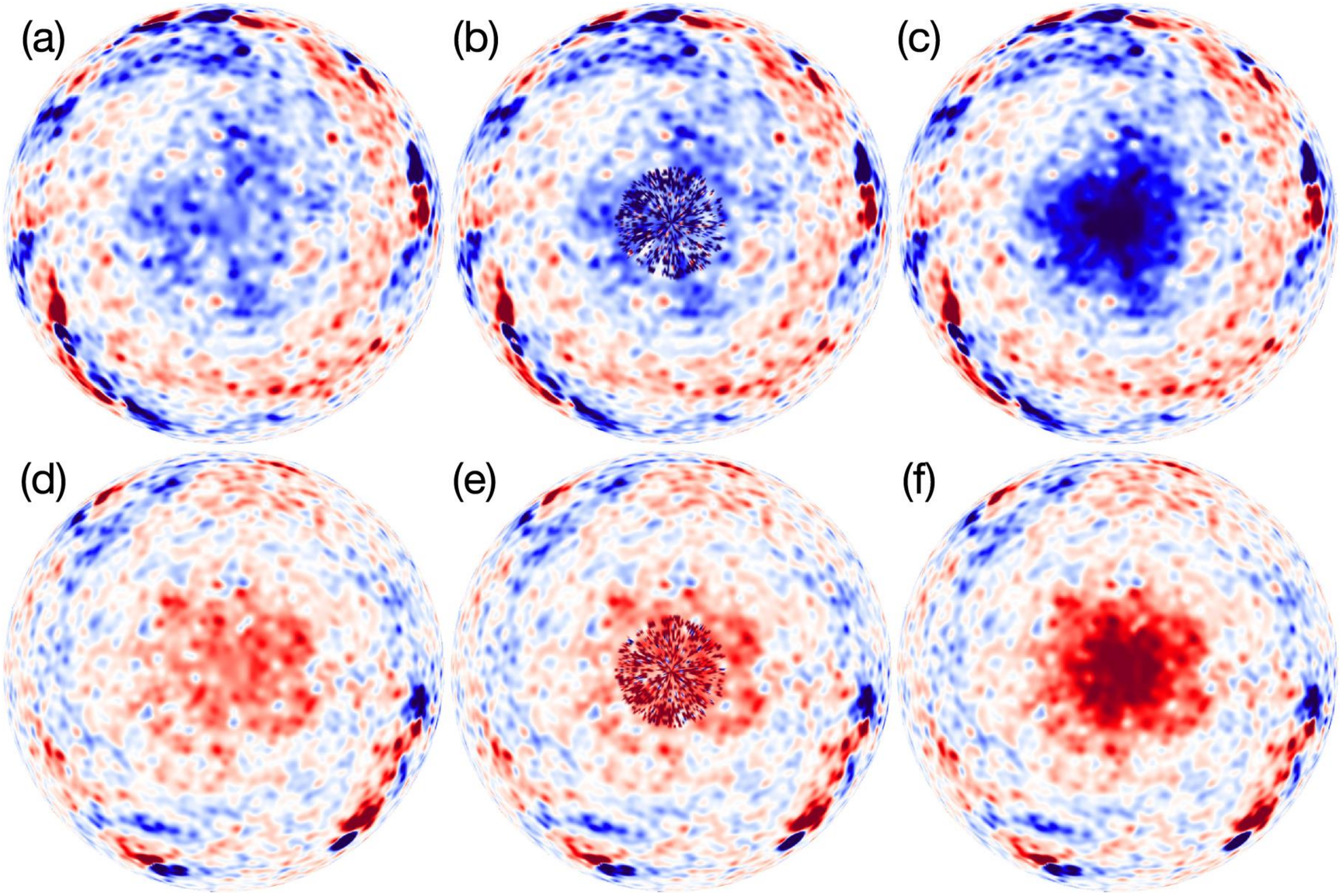

Standard polar field processing

Strong, small-scale fields added at poles

Strong, smooth fields added at poles

Polar view of the radial photospheric magnetic field for CR 2097/2098 (SoHO/MDI data). From Riley et al. (2019).

North pole

South pole

Using potential field source-surface and magnetohydrodynamic models, Riley et al. (2019) demonstrated that the additional polar flux can (at least partially) resolve the open flux problem.

The polar fields have global influence, but difficult to observe from (near) Earth.

- Their magnetic configuration is relatively simple with predominantly near-vertical field lines, but this corresponds to transverse field orientations as seen from Earth, where the polar fields are observed with a large viewing angle.
- The Zeeman effect makes these transverse signals much harder to observe than the longitudinal signals; typically, sensitivity to transverse fields is one order of magnitude lower (Del Toro Iniesta and Martínez Pillet 2012).
- Moreover, the ~kG facular fields that dominate the poles are small (~5″ across as observed from Earth) and sparsely distributed: the overall polar field is only of order 5-10 G.
- This sensitivity problem renders the polar fields relatively poorly constrained in our current modeling efforts.

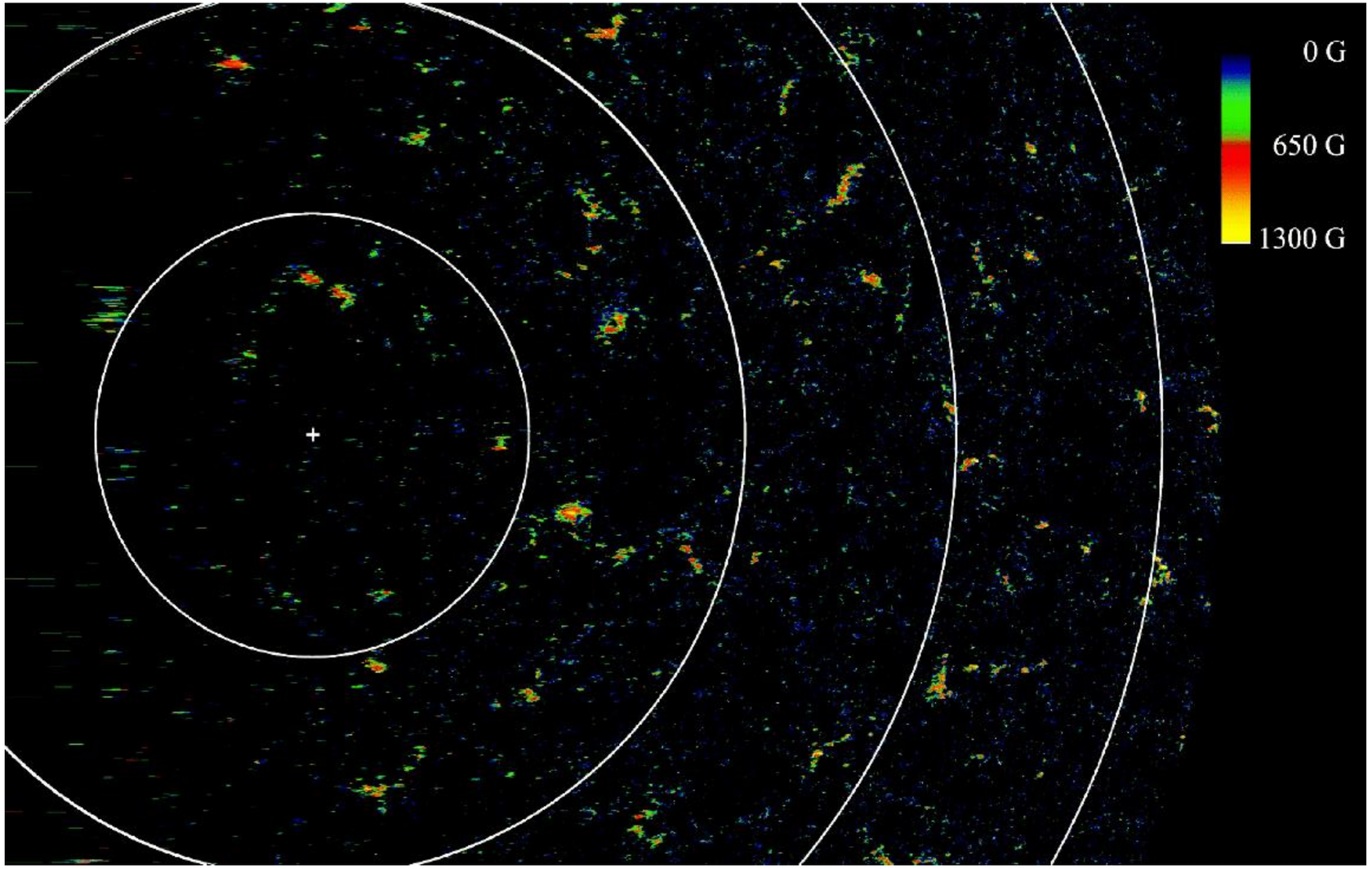

High-resolution observation of the polar field

South polar view of the magnetic field strength taken by Hinode/SOT/SP at 12:02:19-14:55:48 UT on 2007/3/16. East is to the left, west is to the right, and the observation was carried out from the top down. Spatial resolution is lost near the extreme limb (i.e., near the bottom of the figure). The pixel size is 0.16". Latitudinal lines for 85º, 80º, 75º, and 70º are shown as large circles, while the plus sign marks the south pole.

From Tsuneta et al. (2008).

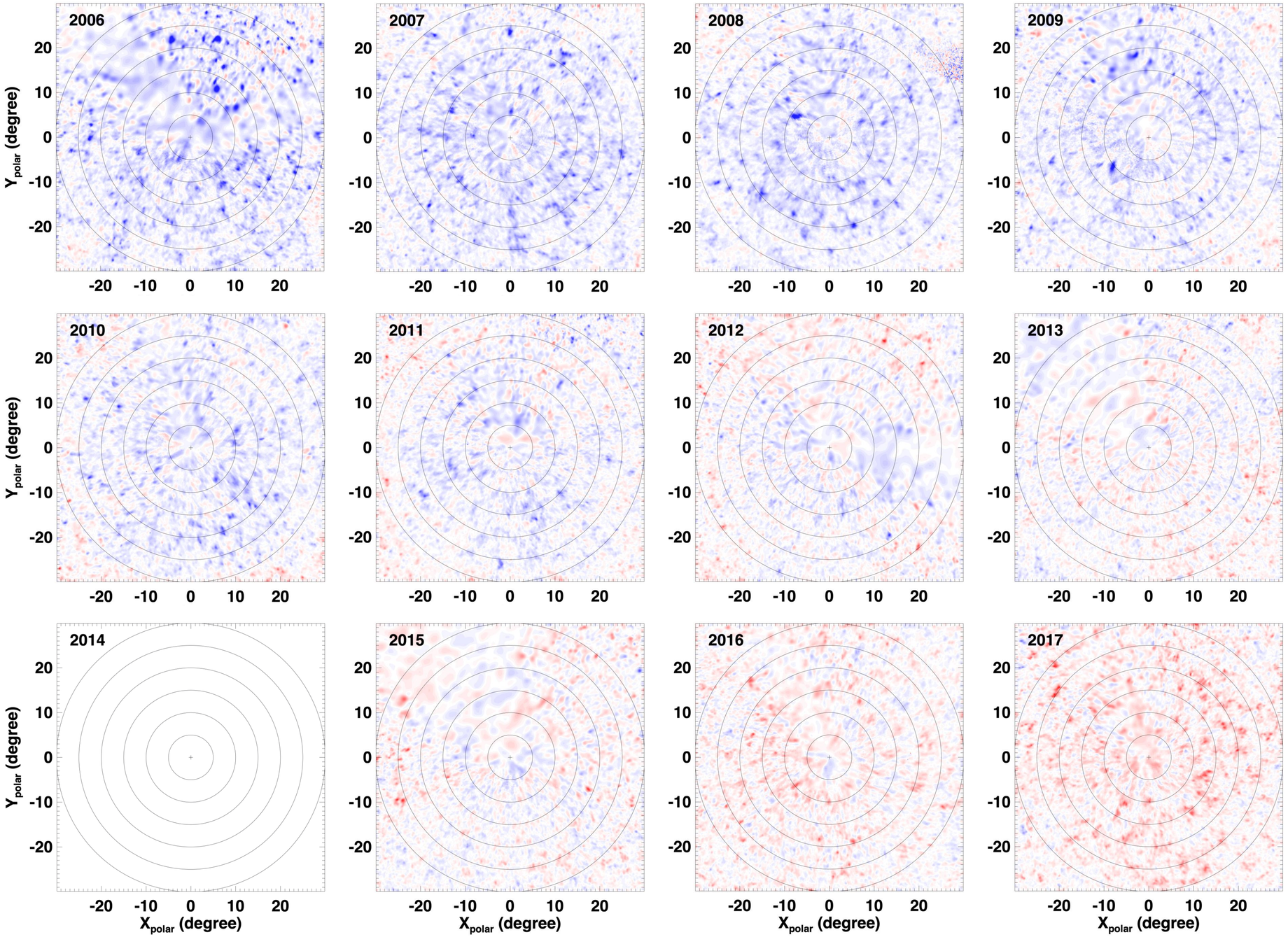

SOLIS/VSM polar maps, LOS data (B_r^{LOS}), north pole

Polar synoptic maps for the north pole covering the years 2006-17.

These maps are based on SOLIS/VSM line-of-sight (LOS) magnetogram observations taken over the 35-day interval centered on the optimal observing day for the north pole, 8 September.

Note the organization of the flux by supergranulation into small, strong concentrations, and the pattern of polarity reversal from lower to progressively higher latitudes.

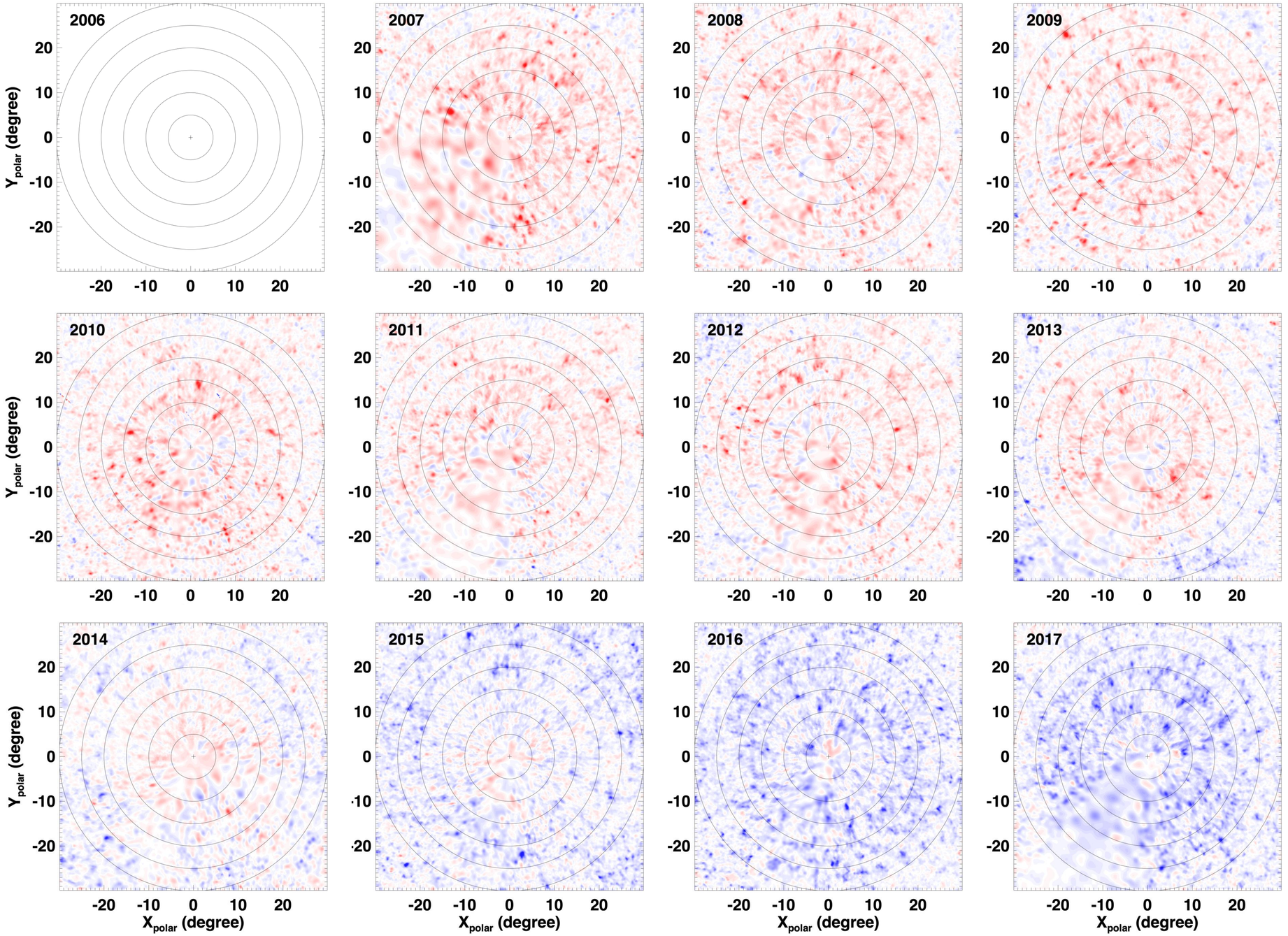

SOLIS/VSM polar maps, LOS data (B_r^{LOS}), south pole

Polar synoptic maps for the south pole covering the years 2006-17.

These maps are based on SOLIS/VSM line-of-sight (LOS) magnetogram observations taken over the 35-day interval centered on the optimal observing day for the south pole, 6 March.

Note the organization of the flux by supergranulation into small, strong concentrations, and the pattern of polarity reversal from lower to progressively higher latitudes.

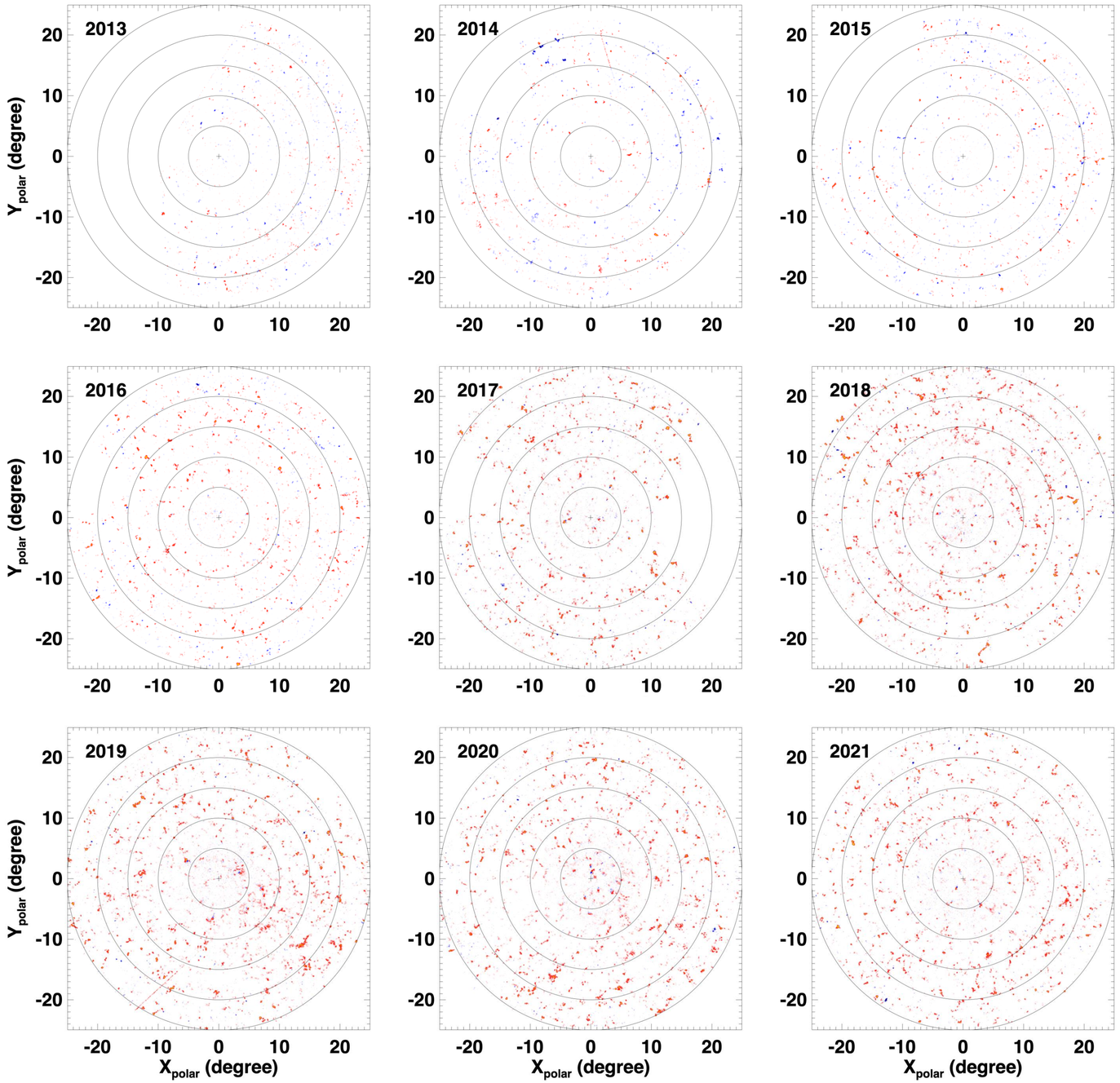

Hinode/SOT/SP polar maps, vector data (B_r^{vec}), north pole

Polar synoptic maps for the north pole from Hinode SOT/SP observations, vector-derived (B_r^{vec}), taken over the 35-day interval centered on the optimal observing day, 8 September, for the north pole.

The organization of the flux by supergranulation into small, strong concentrations is obvious here, but the flux outside these sparsely-distributed concentrations is very weak.

The polar field is observed from near Earth mostly in the transverse component, but the Zeeman effect makes these transverse signals much harder to observe than the LOS signals; typically, sensitivity to transverse fields is one order of magnitude lower.

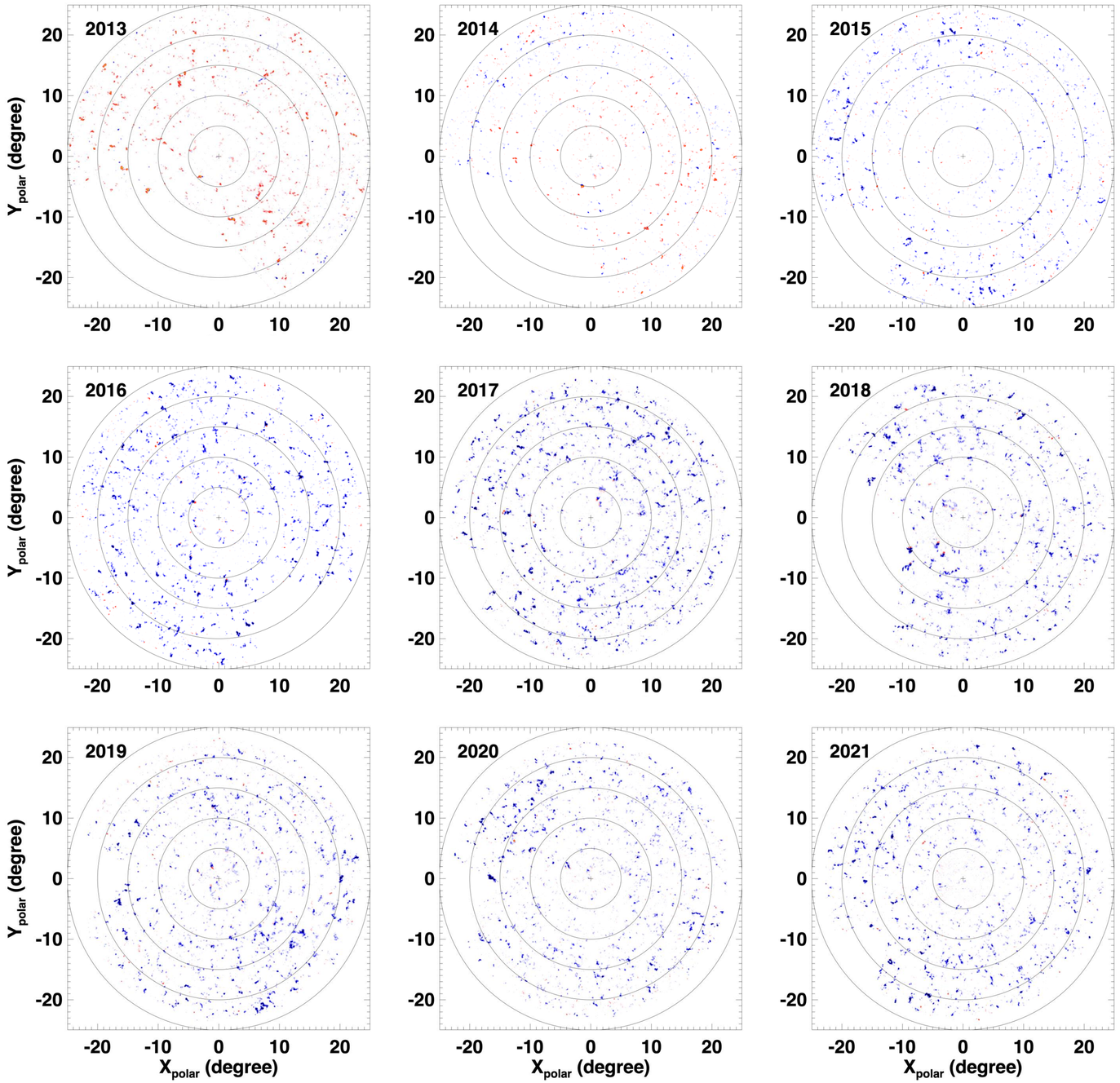

Hinode/SOT/SP polar maps, vector data (B_r^{vec}), south pole

Polar synoptic maps for the south pole from Hinode SOT/SP observations, vector-derived (B_r^{vec}), taken over the 35-day interval centered on the optimal observing day, 6 March, for the south pole.

The organization of the flux by supergranulation into small, strong concentrations is obvious here, but the flux outside these sparsely-distributed concentrations is very weak.

The polar field is observed from near Earth mostly in the transverse component, but the Zeeman effect makes these transverse signals much harder to observe than the LOS signals; typically, sensitivity to transverse fields is one order of magnitude lower.

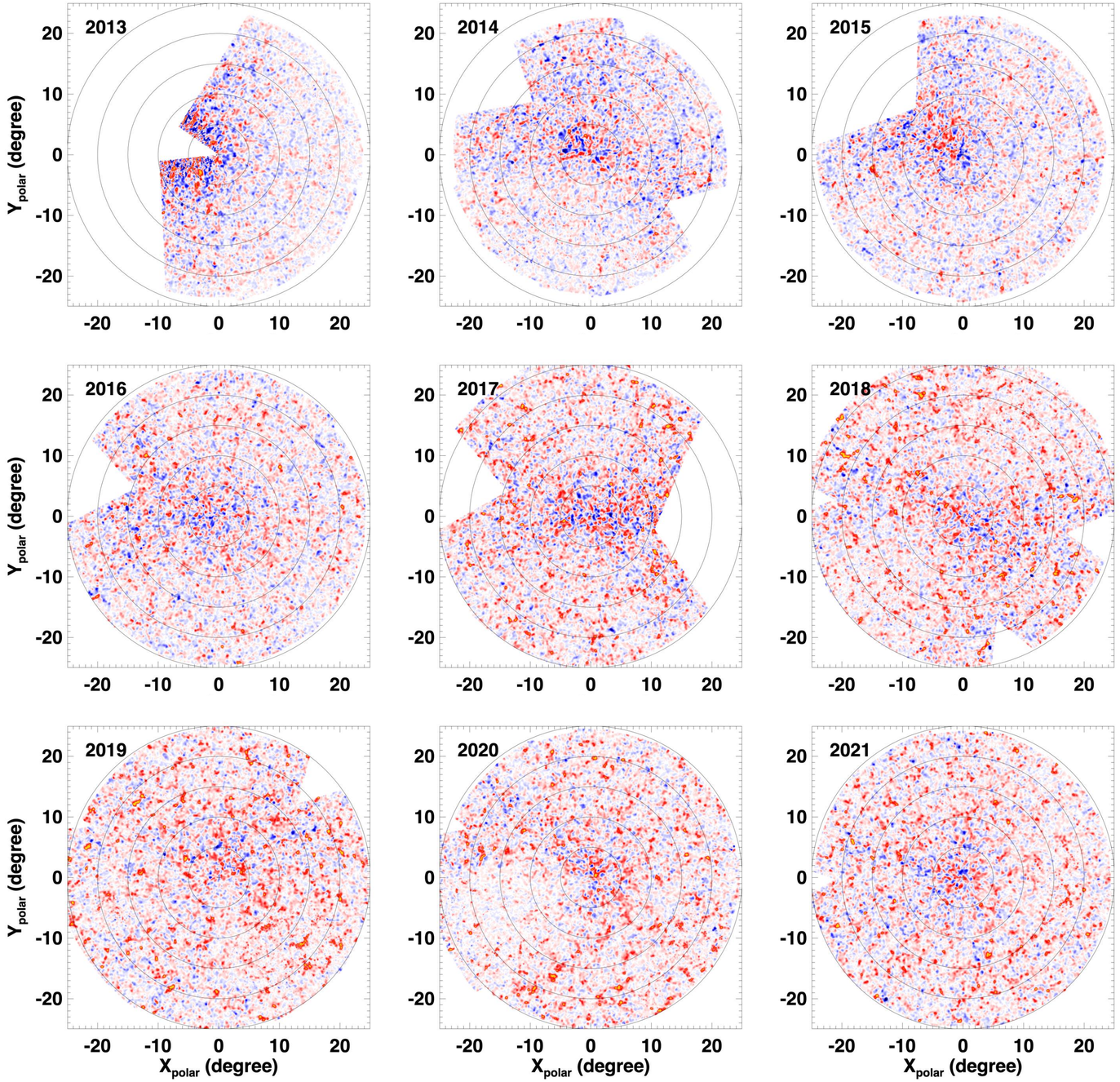

Hinode/SOT/SP polar maps, LOS data (B_r^{LOS}), north pole

Polar synoptic maps for the north pole from Hinode SOT/SP observations, LOS-derived (B_r^{LOS}), taken over the 35-day interval centered on the optimal observing day, 8 September, for the north pole.

The organization of the flux by supergranulation into small, strong concentrations is obvious here, but much more flux outside these sparsely-distributed concentrations is also detected.

Most of the photospheric field is nearly radial, so the radial flux can be estimated from circular polarization (LOS field) measurements alone. The Zeeman effect makes these LOS signals much easier to observe than the transverse signals; typically, sensitivity to LOS fields is one order of magnitude higher.

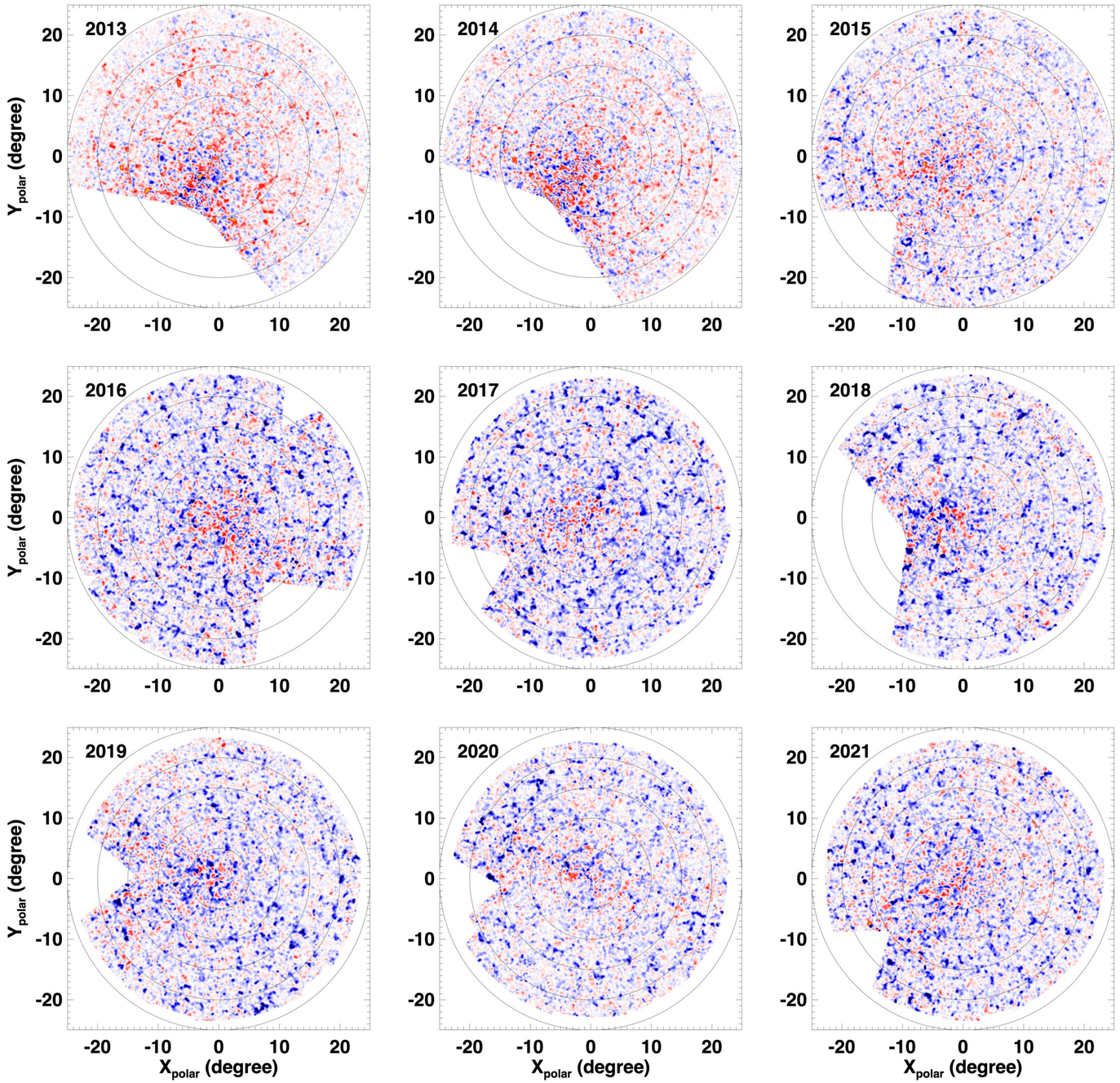

Hinode/SOT/SP polar maps, LOS data (B_r^{LOS}), south pole

Polar synoptic maps for the south pole from Hinode SOT/SP observations, LOS-derived (B_r^{LOS}), taken over the 35-day interval centered on the optimal observing day, 6 March, for the south pole.

The organization of the flux by supergranulation into small, strong concentrations is obvious here, but much more flux outside these sparsely-distributed concentrations is also detected.

Most of the photospheric field is nearly radial, so the radial flux can be estimated from circular polarization (LOS field) measurements alone. The Zeeman effect makes these LOS signals much easier to observe than the transverse signals; typically, sensitivity to LOS fields is one order of magnitude higher.

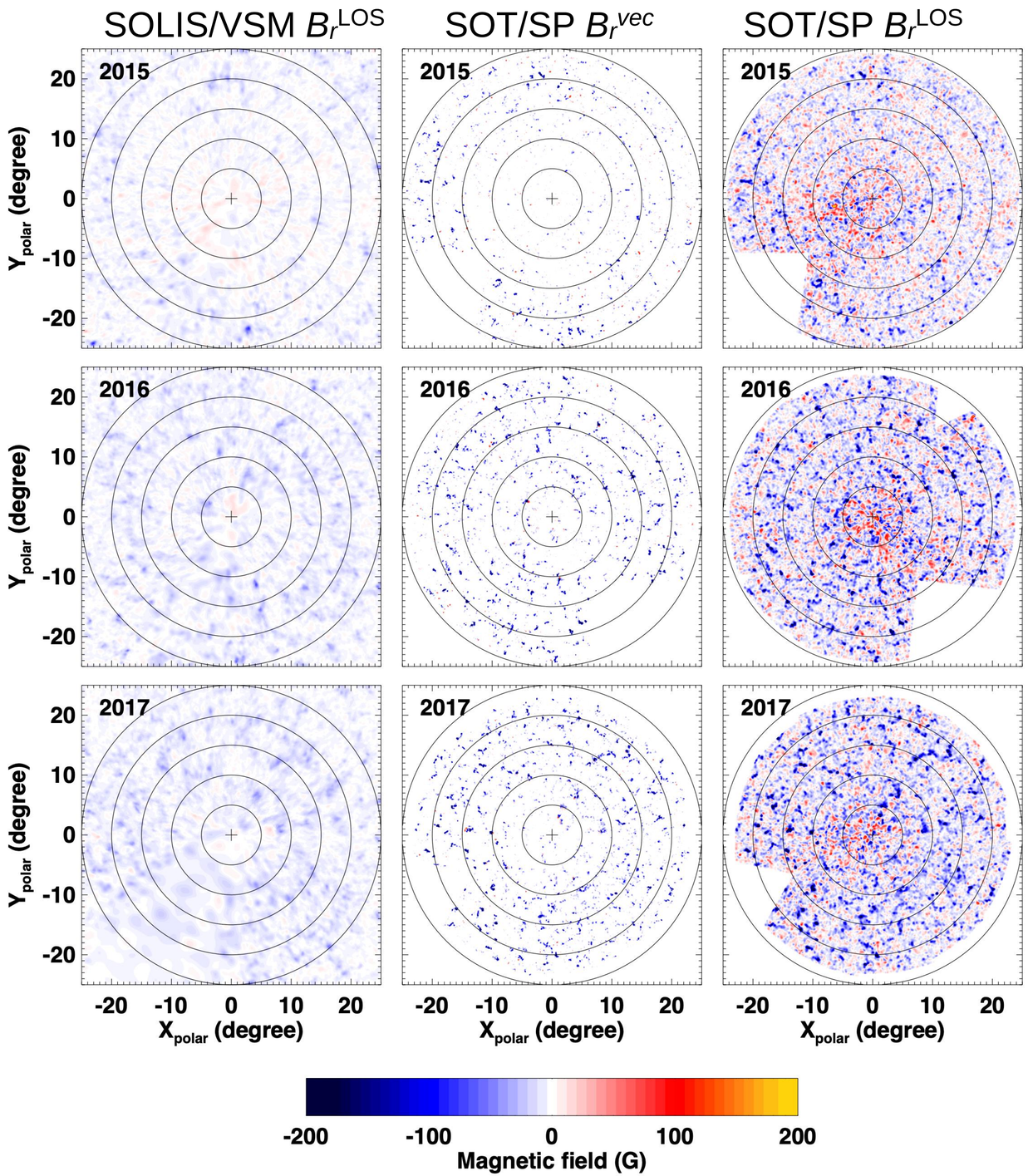

Comparison of SOLIS/VSM B_r^{LOS}, Hinode/SOT/SP B_r^{vec} and SOT/SP B_r^{LOS}.

The VSM and the SP vector- and LOS-derived south polar synoptic maps on a common scale for direct comparison, for three years of overlap between the VSM and SP data sets, 2015-2017.

The flux concentrations are stronger and sharper in In the Hinode data than in the SOLIS data.

The weak fields between the concentrations is stronger in the SOLIS and Hinode LOS-based data than in the Hinode vector-based data.

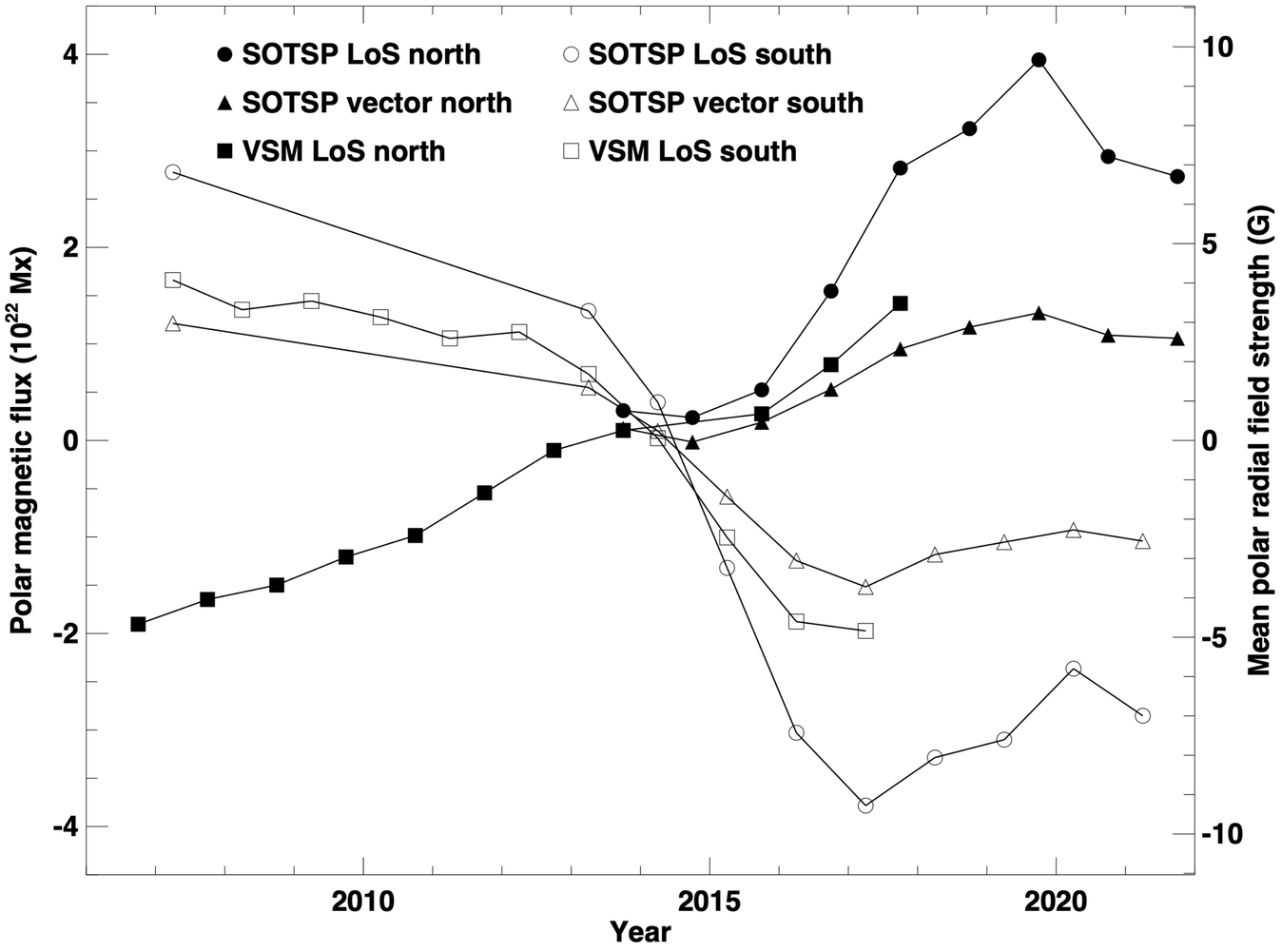

Total polar magnetic flux over time, according to VSM LOS data and SOT/SP vector and LOS data

Estimates of the total net radial magnetic flux through each polar cap as function of time, from the VSM and SOT/SP, when good spatial coverage is available. The polar caps are assumed to extend from the poles to ±60°.

The VSM (2006-2017) and SP (2013-21) have five years of overlap, 2013-17. During these years the SP LOS-based mean radial fields were systematically stronger than the VSM LOS-based fields by a factor of about 2, but the SP vector radial fields were about 20-30% weaker than these VSM fields.

To convert these polar magnetic fluxes to radial IMF contributions at 1 au ≅ 215 $R_\odot$, divide by $2\pi(215\ R_\odot)^2$, and convert from gauss to nanotesla: a 10^{22} Mx polar flux corresponds to a radial IMF of about 0.71 nT implying a typical SOT/SP contribution of about 2-3~nT.

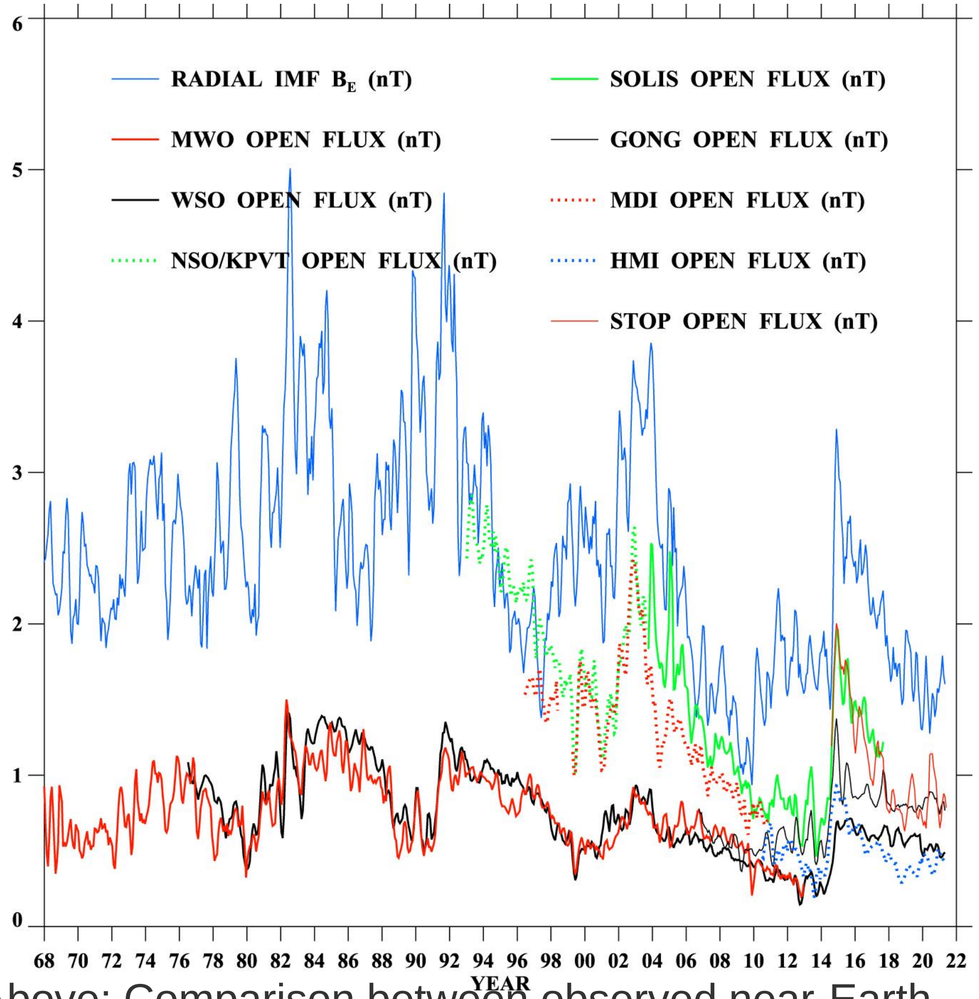

Above: Comparison between observed near-Earth radial IMF strength and PFSS model total open fluxes from MWO, WSO, KPVT/SPM, SOLIS, GONG, MDI, HMI, and STOP synoptic magnetograms. The total unsigned flux crossing the source surface (R_{SS} = 2.5 $R_\odot$) was converted to field strength at 1 au. All curves represent 3-CR running averages.

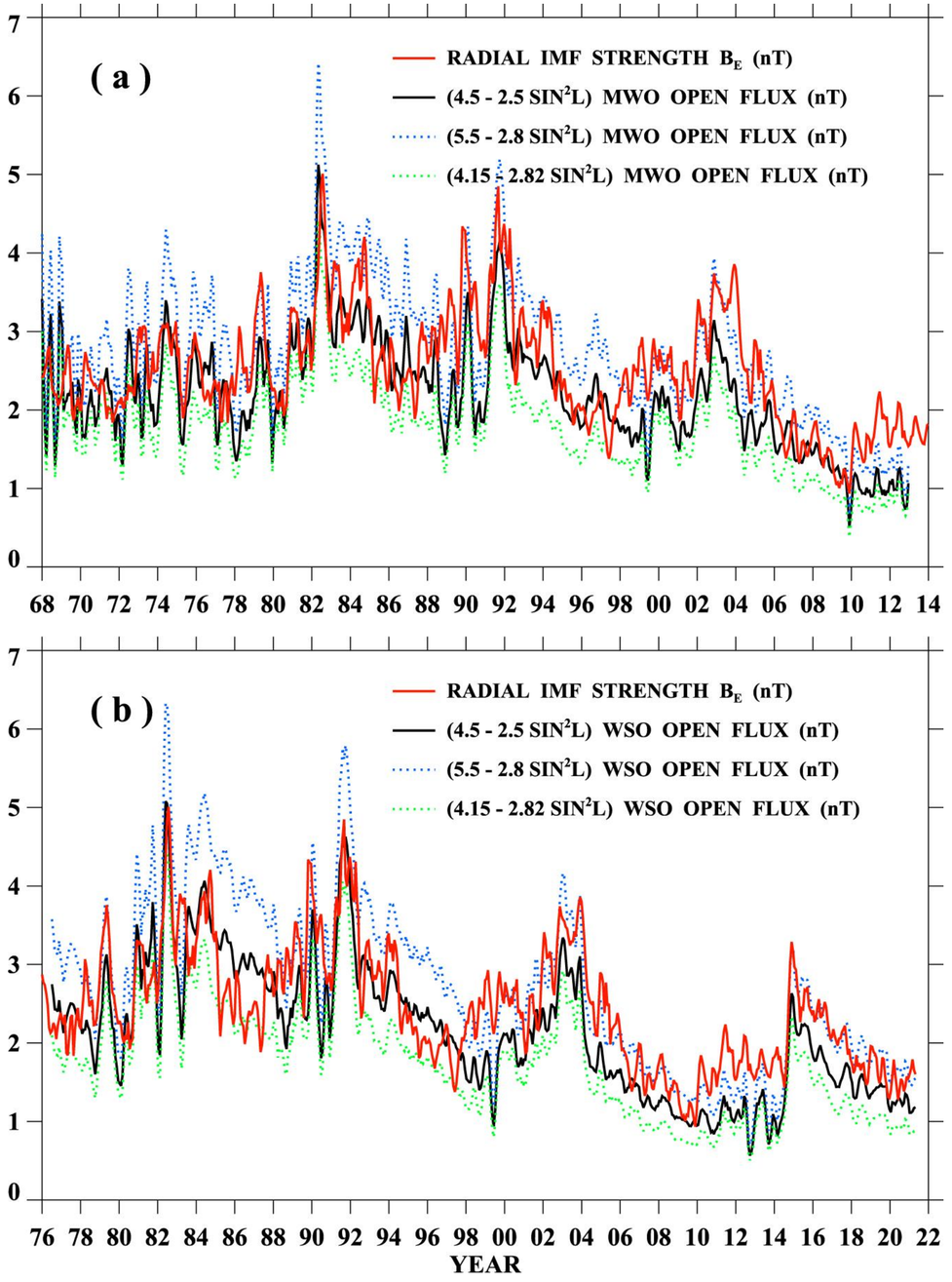

Comparison between observed radial IMF strength and total open fluxes from (a) MWO and (b) WSO synoptic maps, after applying three versions of the Fe I 525.0 nm saturation correction: δ^{-1}=4.5-2.5 sin^{2}L (Ulrich 1992); δ^{-1}=5.5-2.8 sin^{2}L (Ulrich et al. 2009); and δ^{-1}=4.15-2.82 sin^{2}L (Ulrich et al. 2009). The best overall fit is obtained using the δ^{-1}=4.5-2.5 sin^{2}L scaling factor.

Wang et al. (2022)

End-to-end Magnetogram Model

(with V. Martínez Pillet, J. Blanco Rodríguez, and H. Uitenbroek)

We model the HMI magnetogram observation from end to end, simulating the degradation of the signal from diffraction at the telescope aperture to the final inversion for the magnetic field.

Begin with known MHD (MURaM, Rempel 2012, ApJ 750, 62) sunspot simulation data for the magnetic field as “ground truth”.

Compute Stokes spectra for the HMI Fe I 6173 Å spectral line using Rybicki-Hummer (RH) radiative transfer code (Uitenbroek 2001, ApJ 557, 389).

Use Solar Orbiter Polarimetric and Helioseismic Imager Software siMulator (SOPHISM, Blanco Rodríguez et al. 2018), adapted for HMI, to simulate the instrument response to emergent spectra: aperture diffraction, instrument polarization, pixelization, noise, and HMI inversion for line-of-sight magnetic field.

Compare simulated HMI magnetogram with MHD field data, weighted by RH contribution function.

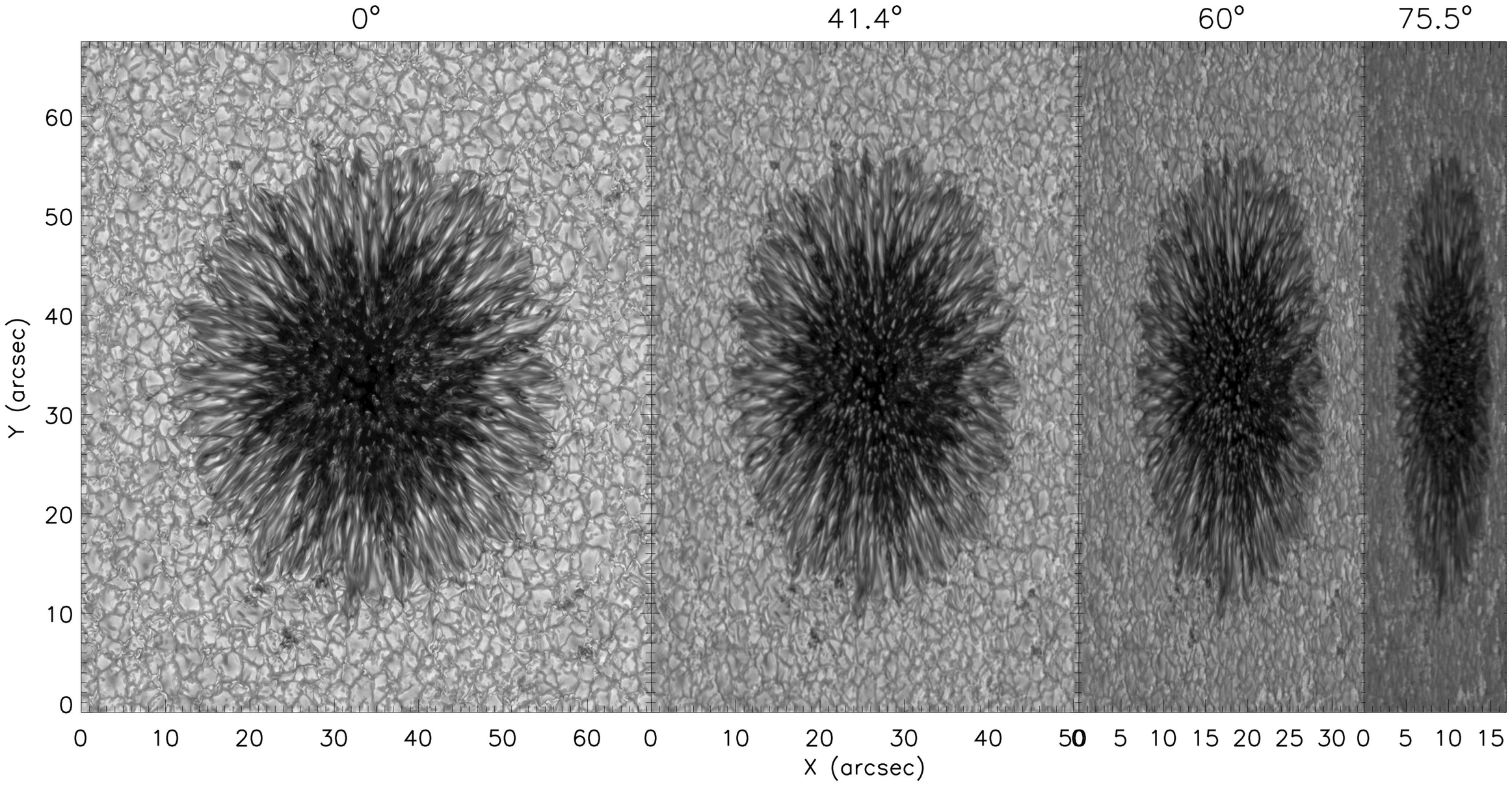

Synthesized continuum intensity images from the four viewing angles, computed using the RH code.

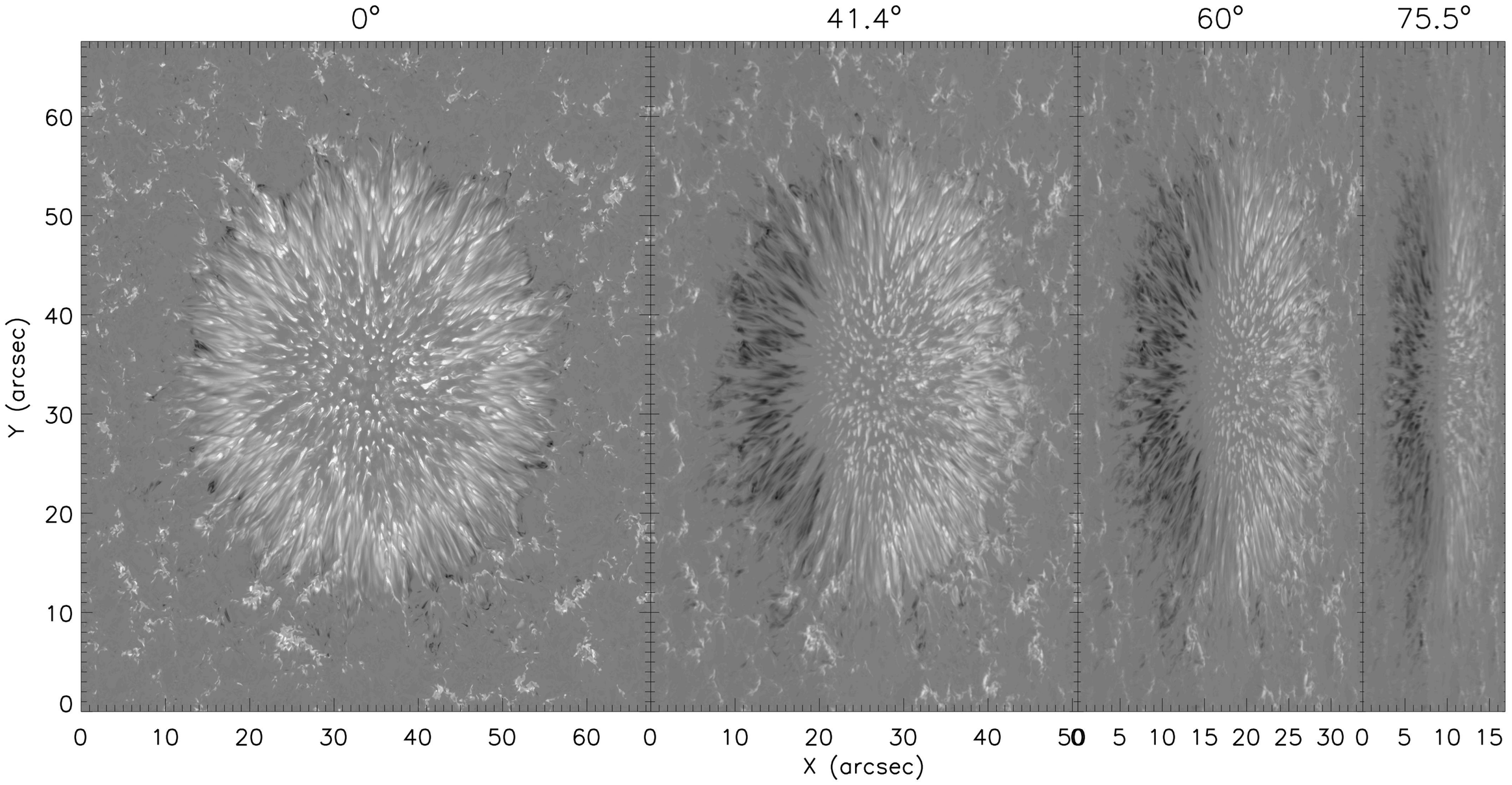

Synthesized Stokes V images, about 0.1Å blueward of nominal line-center, from the four viewing angles.

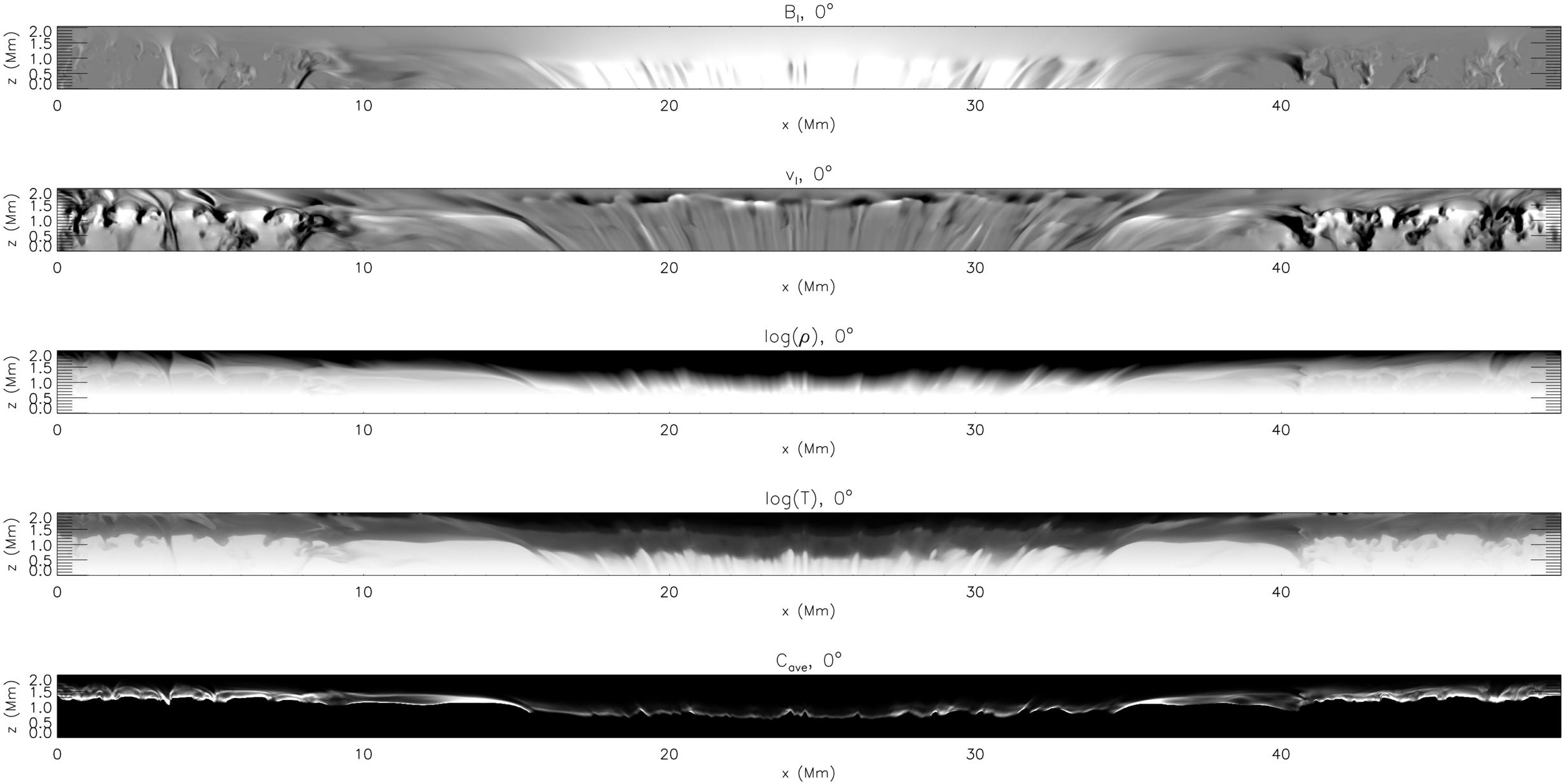

Central x-z planar cuts through the Rempel et al. (2012) sunspot simulation: the 0° line-of-sight magnetic field (top) and velocity, log(density), log(temperature), and the average RH contribution function (bottom).

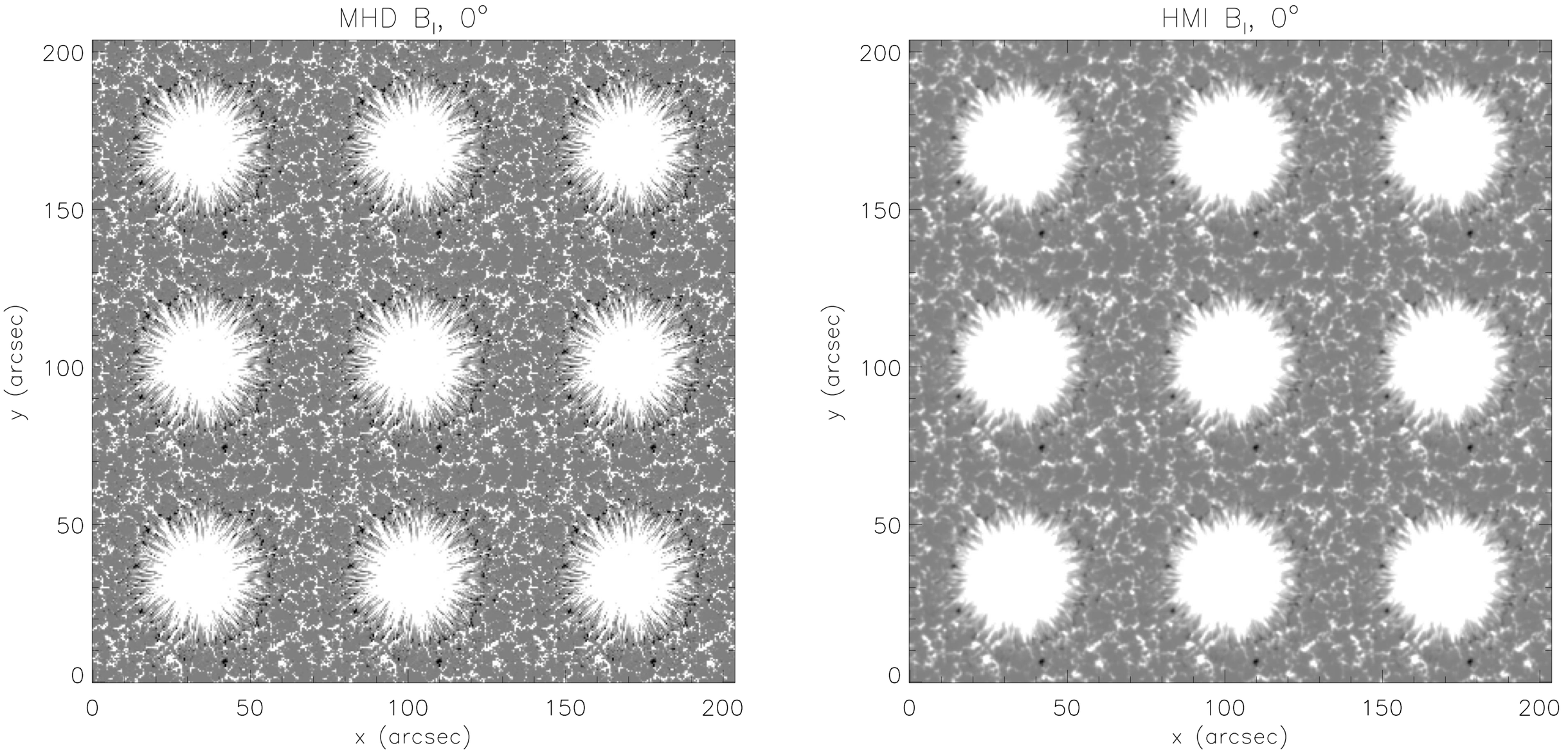

Ground-truth B_l (left) and SOPHISM model HMI B_l (right), for viewing angle 0°. Ground-truth B_l computed as weighted average of MHD line-of-sight component along each line of sight, weighting by contribution function.

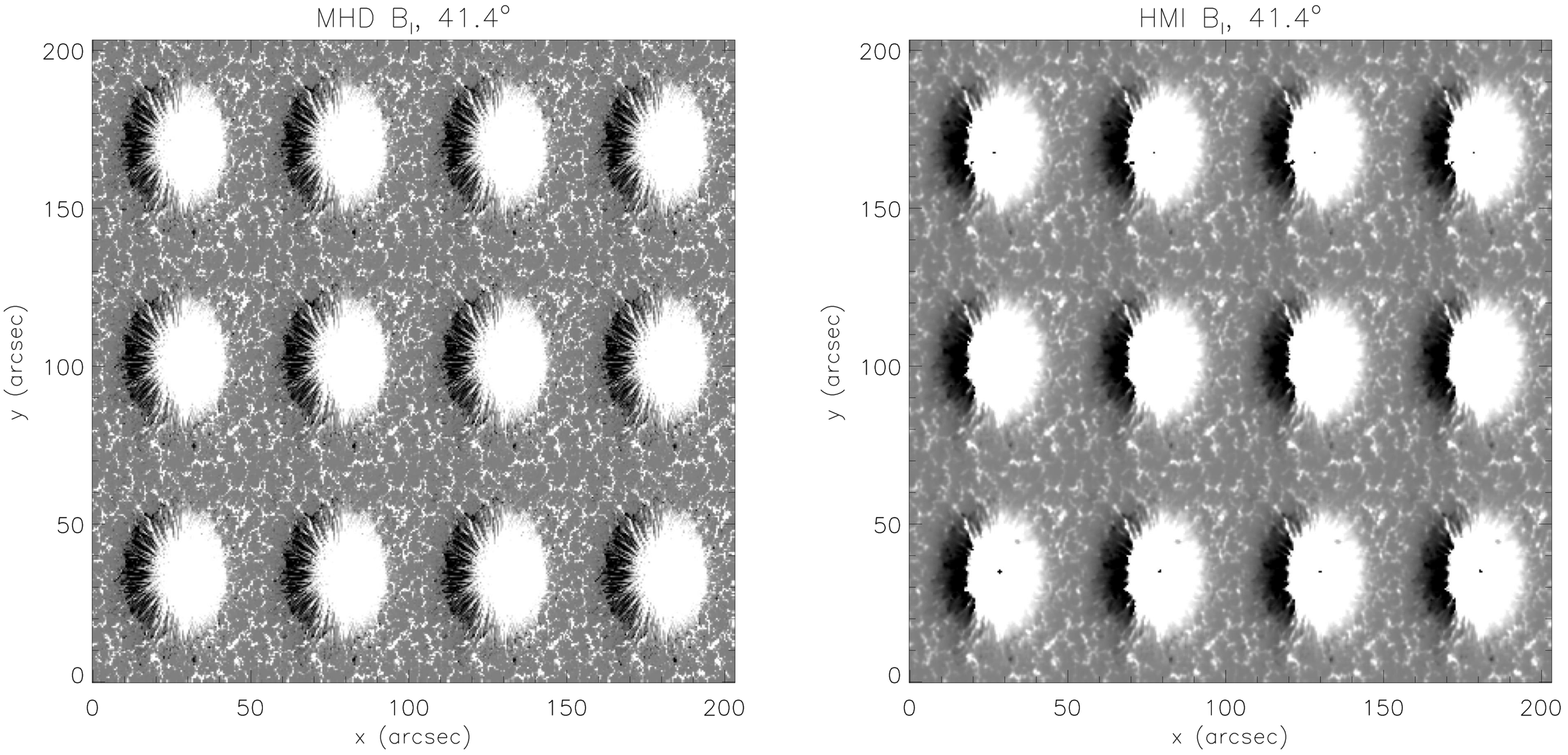

Ground-truth B_l (left) and SOPHISM model HMI B_l (right), for viewing angle 41.4°.

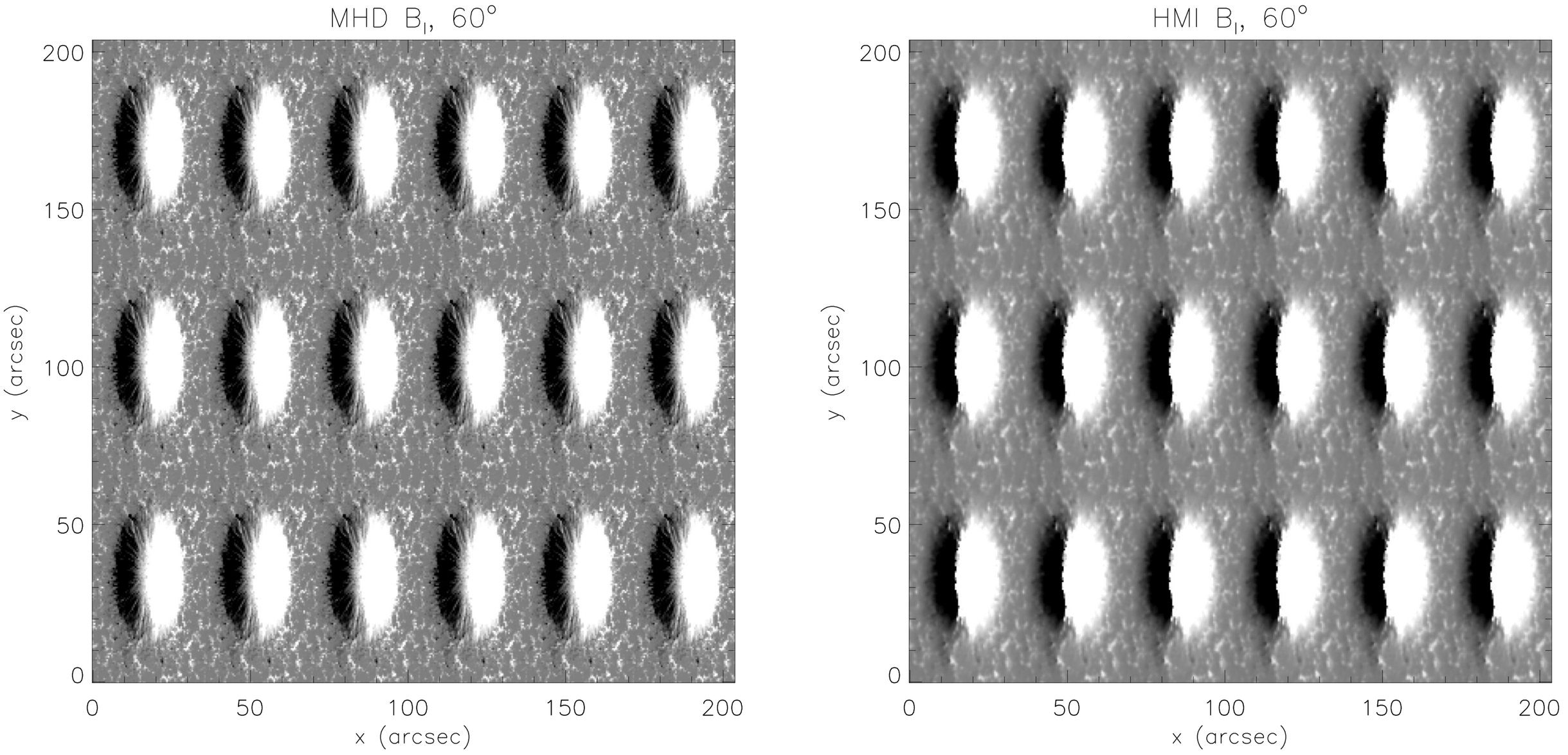

Ground-truth B_l (left) and SOPHISM model HMI B_l (right), for viewing angle 60°.

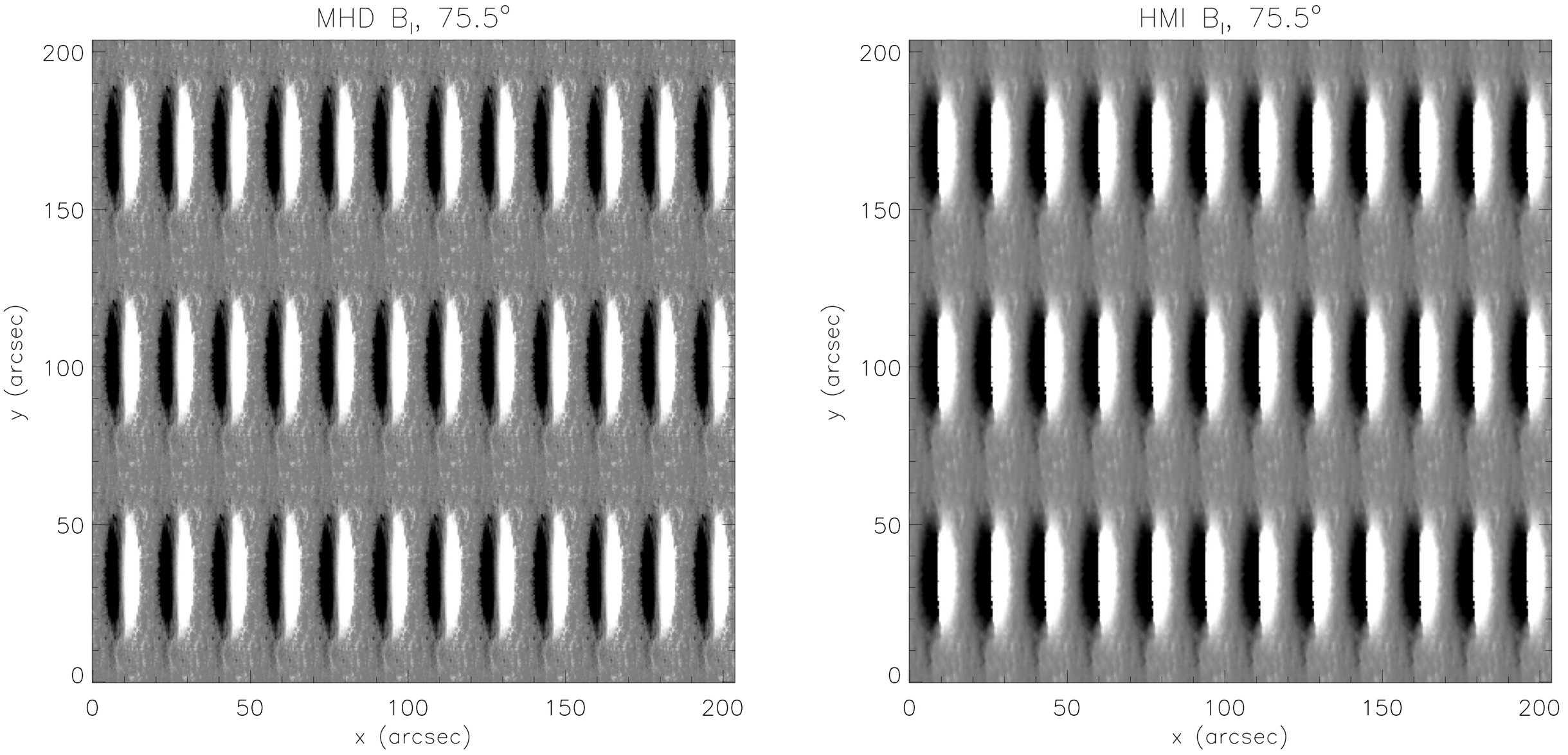

Ground-truth B_l (left) and SOPHISM model HMI B_l (right), for viewing angle 75.5°.

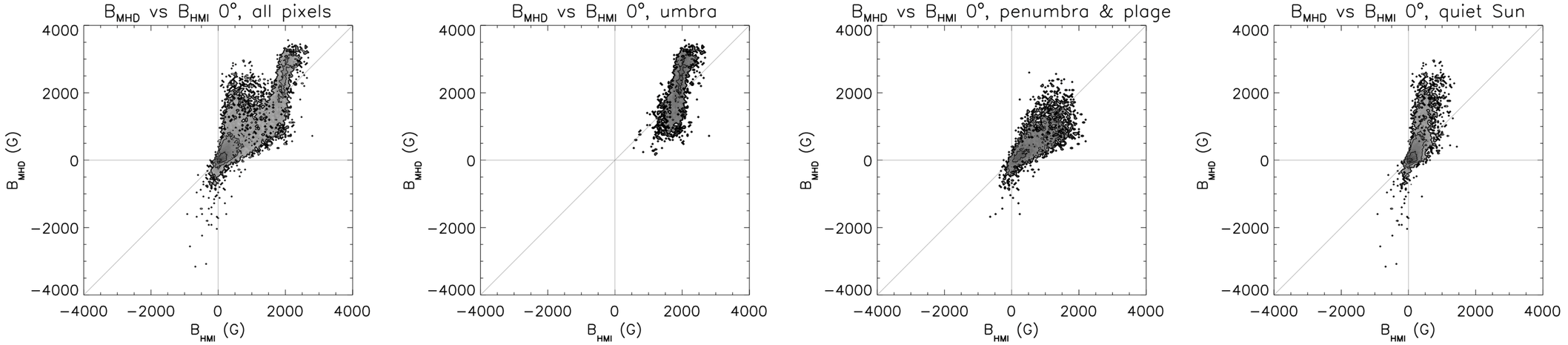

0° viewing angle

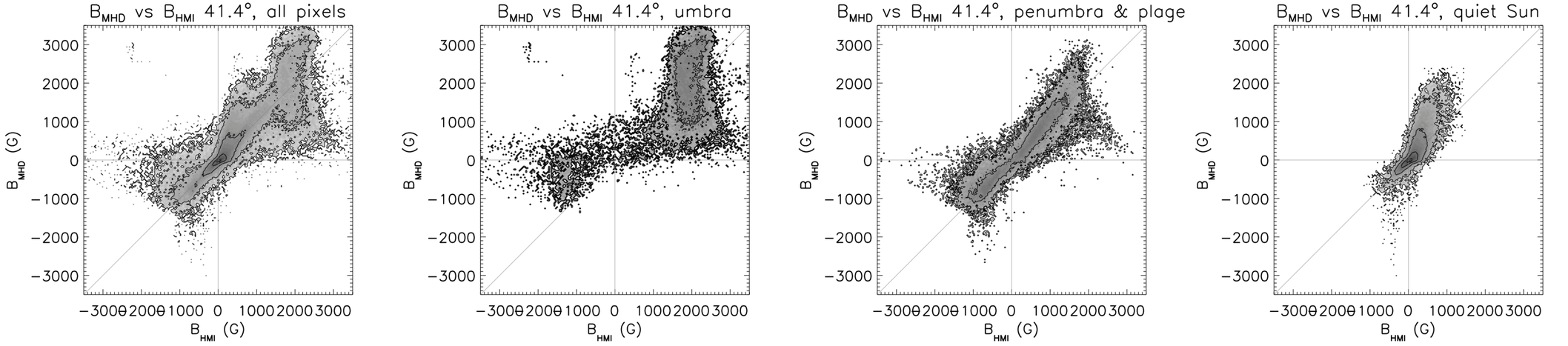

41.4° viewing angle

Scatter plots of ground-truth B_{MHD} vs. modeled B_{HMI}. 1st column shows all pixels, 2nd column umbral pixels, 3rd column penumbral pixels, and 4th column quiet-Sun pixels, selected according to contours on previous slides.

Such scatter plots and curves were derived for the four viewing angles and for selected spacecraft velocities, resulting in lookup tables dependent on field strength, disk position (heliocentric angle) and spacecraft velocity: 3D lookup tables for umbrae, penumbrae, and quiet Sun.

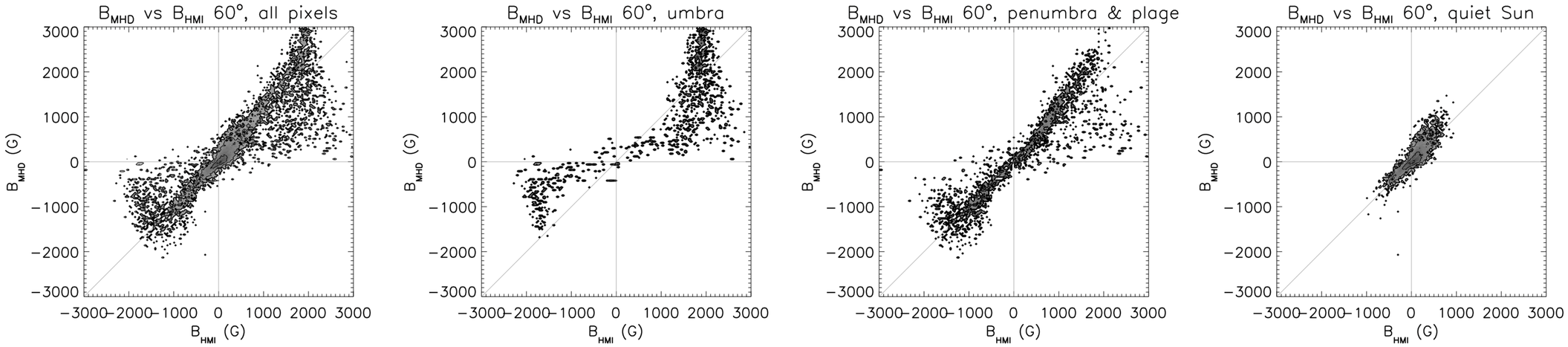

60° viewing angle

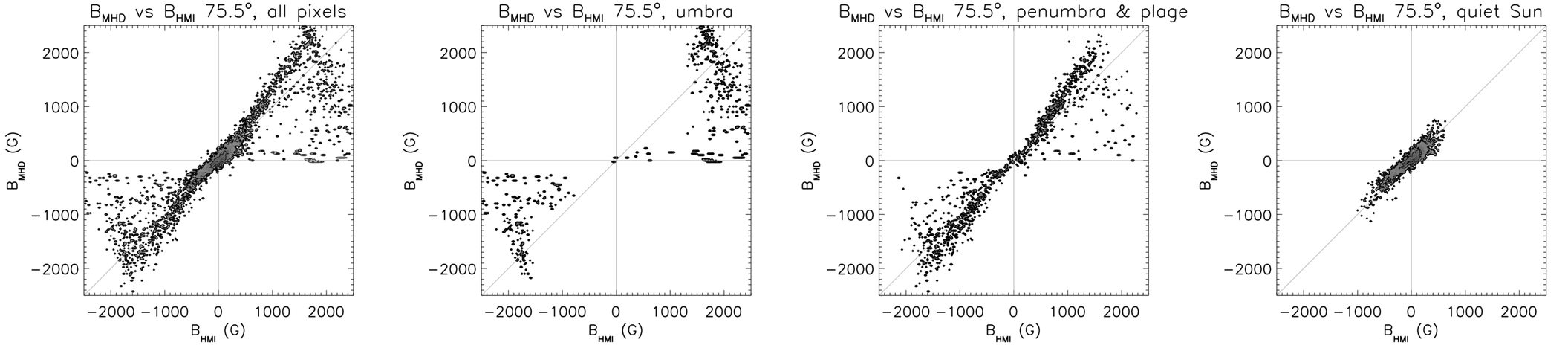

75.5° viewing angle

Scatter plots of ground-truth B_{MHD} vs. modeled B_{HMI}. 1st column shows all pixels, 2nd column umbral pixels, 3rd column penumbral pixels, and 4th column quiet-Sun pixels, selected according to contours on previous slides.

Such scatter plots and curves were derived for the four viewing angles and for selected spacecraft velocities, resulting in lookup tables dependent on field strength, disk position (heliocentric angle) and spacecraft velocity: 3D lookup tables for umbrae, penumbrae and, quiet Sun.

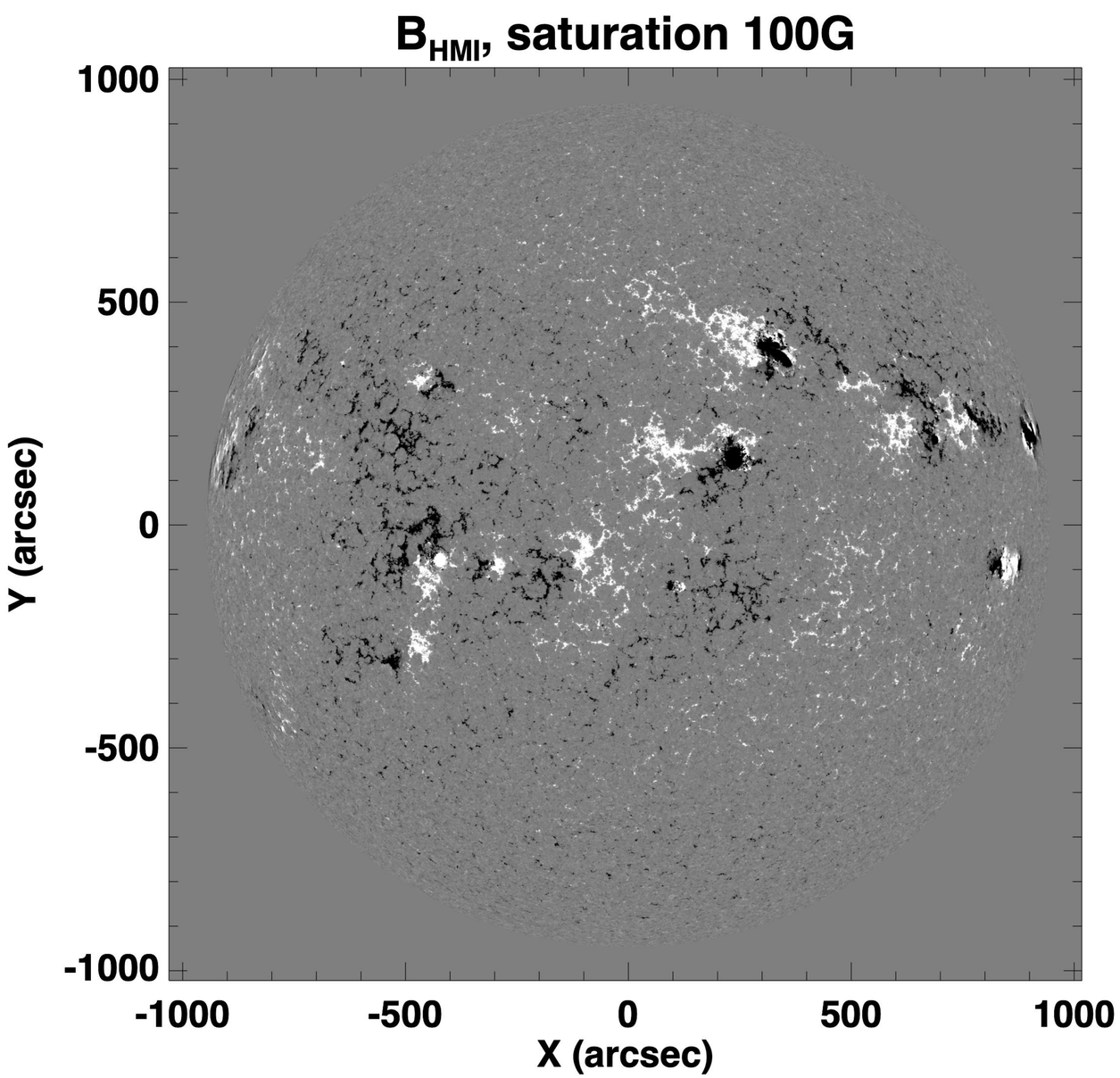

Constructed lookup tables dependent on field strength, disk position (heliocentric angle) and spacecraft velocity, and used them to calibrate HMI data (left).

Below: Ratio of calibrated to uncalibrated $|B_l|$, $|B_l^{cal}| / |B_l^{HMI}|$, as a function of heliocentric angle ρ for a typical image. The calibration factor is largest near disk-center, with some smaller enhancement near the limb.

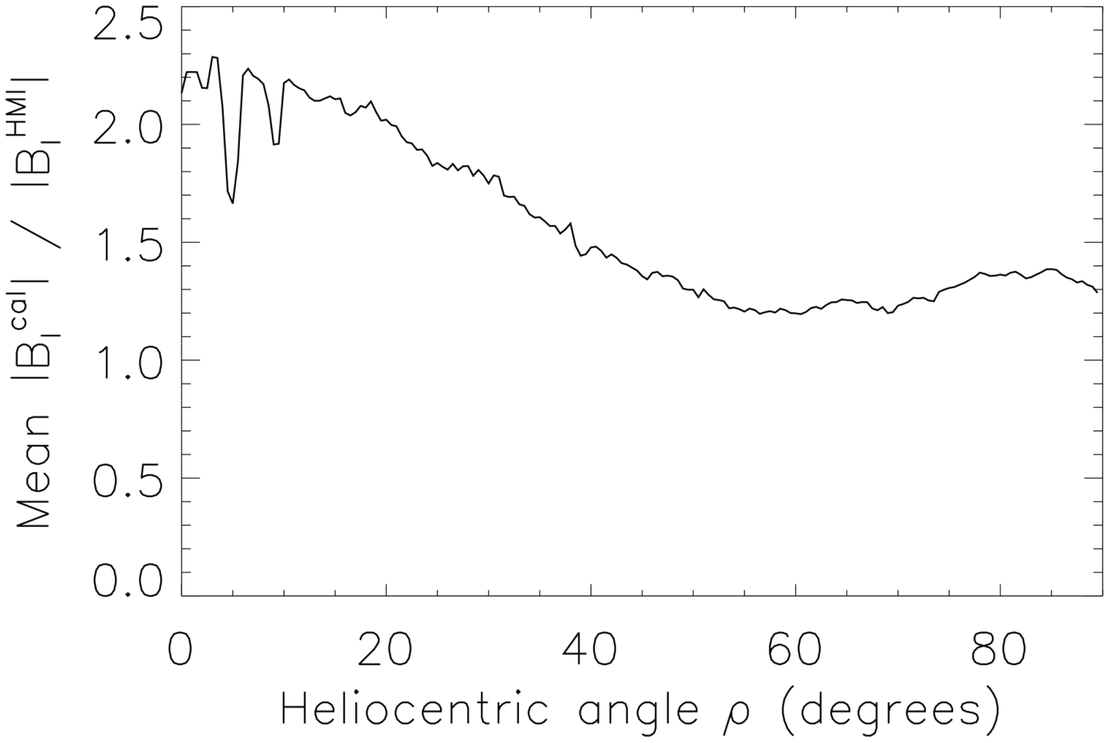

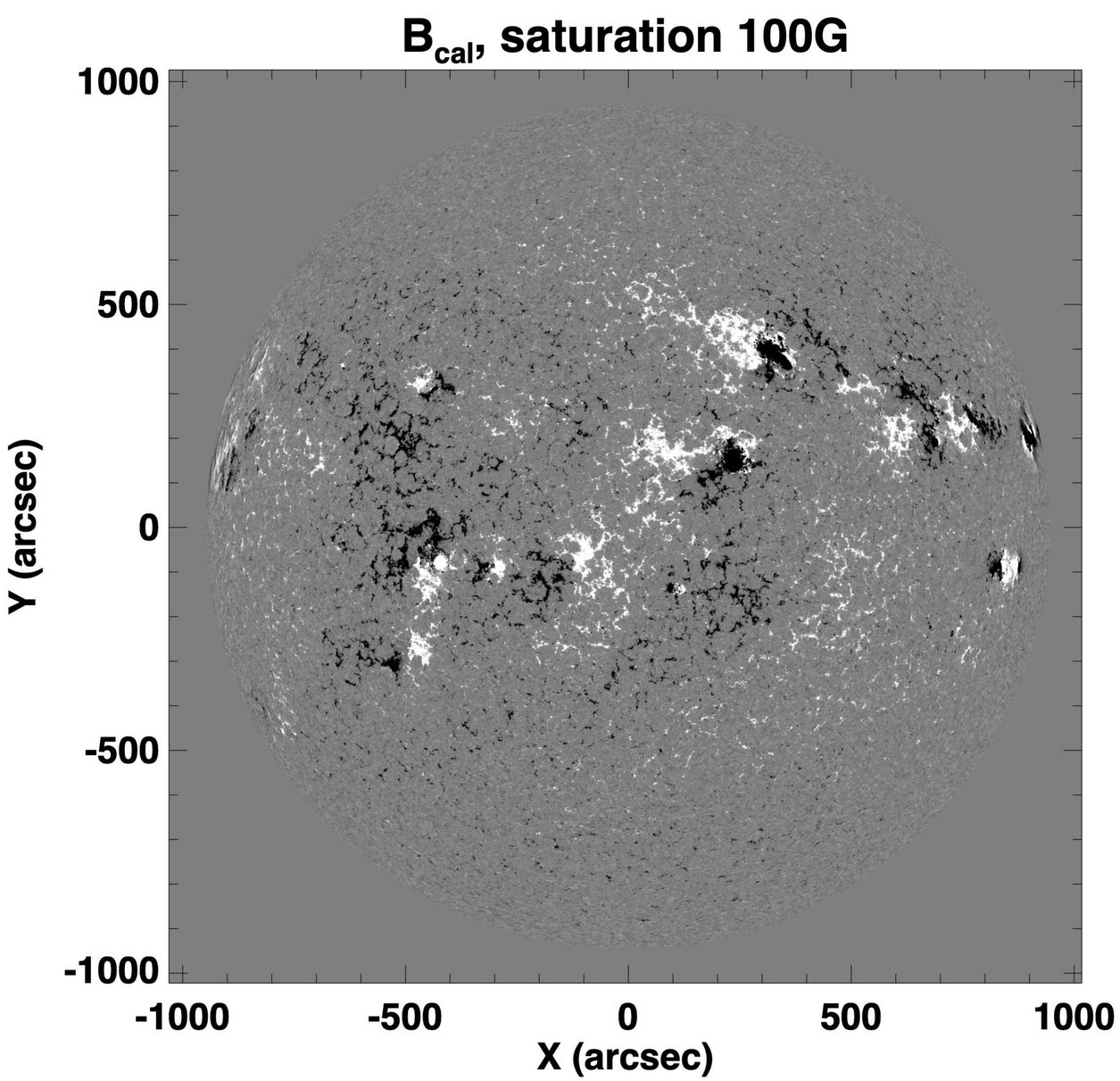

Constructed lookup tables dependent on field strength, disk position (heliocentric angle) and spacecraft velocity, and used them to calibrate HMI data (left).

Below: Ratio of calibrated to uncalibrated $|B_l|$, $|B_l^{cal}| / |B_l^{HMI}|$, as a function of heliocentric angle ρ for a typical image. The calibration factor is largest near disk-center, with some smaller enhancement near the limb.

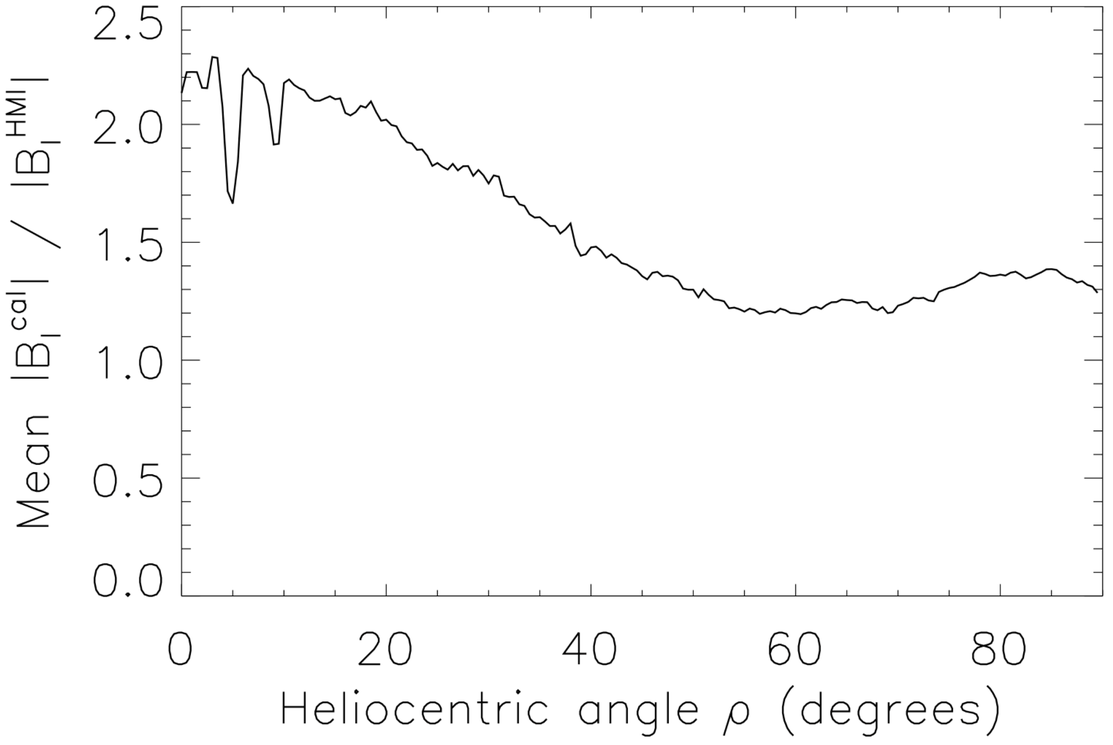

Summary

- Cycle 25 is well under way: the activity is climbing towards solar maximum levels and appears N-S symmetric so far, both polar fields are weakening, and the dipole tilt is quickly heading towards 0° and reversal.
- Full-surface synoptic magnetograms from different sources disagree, especially regarding field strength - and all persistently lead to underestimates of the radial IMF strength. Hinode SOT/SP appears to detect enough LoS field at poles to explain IMF strength, but its full-Stokes vector data suggest a transverse field detection problem for the weaker polar fields. Detect with DKIST, SolO/PHI?
- Derived end-to-end model for HMI magnetogram observation, simulating degrading of solar signal by aperture diffraction, spatial resolution, spectral sampling, & inversion for the field. The resulting calibration factor tends to be largest near disk-center, with some smaller enhancement near the limb - seems too small to solve the ‘open-flux problem’, though this needs to be explored.
- If HMI model works, will apply this method to GONG and SolO/PHI data, test for consistency and usefulness.